Dynamic Light Scattering Unveils Stochastic Degradation in Large-pore Mesoporous Silica Nanoparticles

Valentina Guerrero-Florez,[a] Aude Barbara,[a] Stéphanie Kodjikian,[a] Farid Oukacine,[b] Philippe Trens,[c] Xavier Cattoën[a,]*

[a] Univ. Grenoble Alpes, CNRS, Grenoble INP, Institut Néel, 38000 Grenoble, France.

[b] Univ. Grenoble Alpes, DPM, CNRS UMR5063, F-38041 Grenoble, France

[c] ICGM, Univ Montpellier, CNRS, ENSCM, Montpellier, France

Corresponding author: xavier.cattoen@neel.cnrs.fr

Phone: +33476881042

Abstract

Mesoporous Silica Nanoparticles (MSNs) have been increasingly investigated as versatile drug delivery carriers. A particular challenge for the systemic use of MSNs lies in the control of their degradation, which has not been fully understood until now. We implemented standard dynamic light scattering (DLS) experiments and introduced a novel DLS technique in a confocal volume to track the dynamics of large-pore MSN degradation *in situ*. This unique DLS technique, which involves a small observation volume, was chosen for its ability to count particle by particle during the degradation process, a method that has not been commonly used in nanoparticle research. The experiments were performed in different media compositions at low particle concentrations, below the silica solubility limit. MSNs with large conical pores were prepared and studied as they offer the possibility to incorporate and release large-sized biomolecules. Large-pore MSNs followed a singular degradation mechanism following a stochastic-like behavior, a finding that challenges the common idea that all nanoparticles (NPs) degrade similarly and homogeneously over time. We showed that some NPs are observed intact over a prolonged period while most other NPs have already vanished or been transformed into swollen NPs. Thus, a heterogeneous degradation process occurs, while the total concentration of NPs undergoes an exponential decay. These large conical pores MSNs will be utilized as reliable biomolecule nanocarriers by predicting the factors underlying the NP hydrolytic stability.

Keywords: Large-pore mesoporous silica, drug delivery carrier, degradation, surface modification, DLS.

Abbreviations: MSN: Mesoporous Silica Nanoparticle; DLS: dynamic light scattering; NP: nanoparticle; SEM: scanning electron microscopy; CTAB: Hexadecyltrimethylammonium bromide; CTAC: hexadecyltrimethylammonium chloride; TEOS tetraethyl orthosilicate, MPTMS: (3-mercaptopropyl)trimethoxysilane; TEOA: triethanolamine; TIPB: 1,3,5-Triisopropylbenzene; PBS phosphate-buffered saline; TPOS: Tetrapropyl orthosilicate.

1. Introduction

Over the past decade, the materials science community has given considerable attention to the use of mesoporous silica nanoparticles (MSNs) in biomedicine owing to their large surface area (700-1000 m^2 g^{-1}), elevated pore volume (0.6-1.0 cm^3 g^{-1}), and adjustable pore size (2-5 nm).[1–3] In light of drug delivery applications, MSNs became an outstanding alternative to conventional polymer- and lipid-based nanocarriers due to their rigidity, dispersibility, biocompatibility, and accessible surface modification, incorporating numerous functionalities.[4,5] Large-pore MSNs, with their unique advantages in encapsulating macromolecules, offer a promising future in drug delivery. They can transport therapeutic molecules to specific targets for disease treatment with high efficacy, allowing for decreased dosage and frequency, thereby preventing toxicity issues.[6–8] The large pore structure of MSNs provides an ideal environment for fast diffusion, making them convenient and practical nanocarriers.[9] Consequently, a precise design of the mesostructure architecture with a short diffusion length and enlarged pores can improve biomolecule transport.

MSNs have a distinct advantage over other porous inorganic materials. They can degrade by hydrolysis under physiological conditions, making them a confident choice for drug delivery applications.[10,11] Nevertheless, understanding their degradation behavior is crucial for optimizing their stability and ensuring the successful delivery of therapeutic molecules. Preferably, an MSN-based nanocarrier should be stable enough to load and transport intact cargo to the target place, avoiding premature release yet labile enough to be biodegradable and minimize potential toxicity concerns. In several studies, MSN degradation was evidenced within the first 24 hours in aqueous media at very low concentrations. [12,13] It is worth noting that the time scale of the degradation kinetics varied vastly depending on the experimental conditions, leading to miscellaneous and inconsistent scenarios on the degradation of MSN. [14,15]

Overall, the dissolution outcome of amorphous silica can be described as a stepwise mechanism that involves hydration, hydrolysis, and ion exchange of the siloxane framework to finally form silicic acid, the main product of silica degradation [10,11,16]. The kinetics and thermodynamics of the reaction are driven by the solubility limit of silica. Above this limit, dissolved silicate species can undergo re-precipitation from the saturated medium, negatively impacting the pore structure and surface area. Under equilibrium, this process might lead to particle aggregation [17]. However, under this limit, only silicic acid and oligomers should be formed, with no more material in solution. The main parameters controlling the degradation kinetics of MSN are the medium composition, particle concentration, and physicochemical and textural properties of the particles. Investigations have been carried out to assess the role of such parameters in the degradation of MSNs and, most importantly, to predict their biological outcome. Even though the importance of studying the degradability of silica-based nanomaterials has been recognized, there are only a few articles primarily dealing with the hydrolytic degradation of large-pore MSNs, notably when highly diluted colloids in aqueous media are considered far from saturation

condition, such as those used in drug delivery applications.[18–20] The aggregation and degradation of silica nanoparticles (NPs) in different biologically relevant media have been recently reviewed, summarizing the most recent work assessing the colloidal stability of MSNs.[10] Various MSNs have been studied through synthesis routes, morphologies, degree of structural order, particle size, and pore size. Although these works show the influence of biological fluids on the colloidal stability of MSNs, a systematic conclusion based on literature data is not possible as conditions vary widely between the different reports, and only a few studies properly report the actual experimental conditions used. The synthesis conditions under which the materials are produced strongly influence the silica framework connectivity. Some synthetic methods lead to a high degree of six-fold cyclic silica species, typically more reactive towards hydrolysis than linear bonded silica species.[21] This structure-dependence reactivity led to various possible scenarios explaining conflicting data on the mechanism and kinetics of degradation of MSNs in biologically relevant conditions found in the literature. Nonetheless, the data has been valuable to gain insight into critical factors that govern MSN stability. Chiefly, two leading families of actors have been found to govern the degradation rate of silica:[11,17,22] (i) structural-textural parameters (involving morphology, porosity, condensation degree of the silica network, surface chemistry, etc.) and (ii) the properties of the surrounding medium (pH, concentration, additives, etc.). Consequently, the degradation kinetics of MSNs in aqueous media can widely vary from hours to several weeks, depending on their physicochemical properties. Several works have been carried out to assess the influence of the parameters mentioned above on the hydrolytic stability of MSNs, such as size,[23] specific surface area,[24] concentration,[19,20,24] siloxane cross-linking,[25] or organic functionalization.[26]. Despite several studies on MSN degradation *in vitro*, the degradation outcome of large-pore MSNs has been scarcely studied.[25,27] To the best of our knowledge, no reports addressing *in situ* the degradation mechanism of large-pore MSNs have been reported until now. In particular, the pore structure plays a crucial role in the degradation, not only for the inherent enhancement of surface area but also for the rapid diffusion of molecules within the large pores. Therefore, it is relevant to account for the changes in the mesostructure and the general colloidal behavior of the particles upon degradation.

In order to shed new light on the degradation mechanisms of large-pore MSNs, we present here a novel method for evaluating MSN degradability, combining two dynamic light scattering (DLS) techniques, allowing to monitor the degradation kinetics. The unique feature of confocal-volume DLS, which enables to monitor and count particles during degradation, provides a more comprehensive understanding of the overall behavior. We have developed an analytical approach to use this method in conjunction with conventional DLS, electron microscopies, and nitrogen sorption to establish the relationship between MSN structural parameters, dissolution media composition, and dissolution kinetics. In parallel to this study, we compared the degradation kinetics of common purely siliceous large-pore MSNs and hybrid organosilica containing covalently linked mercaptopropyl moieties (large-

pore MSN-SH). This unusual technique enables the determination of critical parameters such as concentration and number of particles at different degradation stages, thereby providing a comprehensive understanding of MSN degradation.

Although large-pore MSNs seem desirable nanocarriers, preparing well-dispersed, uniform MSNs with enlarged pores represents a considerable challenge in sol-gel surfactant-templated synthesis. Here, large-pore MSNs with controllable particle and pore sizes were successfully synthesized under neutral or basic pH *via* two synthetic routes developed by Kuroda's [28] and Bein's [29] research groups (denoted as *k*-MSN and *b*-MSN, respectively). A modification of these synthetic approaches was done to functionalize MSNs by a co-condensation process in a multistep growth method, which allowed us to achieve a spatially selective anchoring of mercaptopropyl functional moieties on the outer surface of MSNs while preserving their dispersibility. Notably, as-prepared *k*-MSNs and *b*-MSNs are spherical, highly monodisperse, and exhibit outstanding colloidal stability. In this regard and to gain a comprehensive view of the role of the structural order on the dissolution kinetics of large-pore MSNs, we compared the degradation of *k*-MSNs and *b*-MSNs in pure water and PBS at 37 °C by using a low particle concentration of 0.1 $mg \cdot mL^{-1}$.

Remarkably, we deciphered an unexpected stochastic degradation behavior on large-pore MSNs. This degradation pathway proceeds heterogeneously, while morphological changes were observed where the mesopores evolved from isolated conical to swollen, interconnected. The coexistence of these two populations of particles during the first 3 hours and a sharp decrease in the number of particles was found by following the dissolution process under low particle concentration by *in situ* DLS techniques and electron microscopies. We showed that the dissolution profile of MSNs can be finely tuned by modifying the structural properties of the MSNs, such as surface functionalization and pore density. The mercaptopropyl-functionalized shell can effectively whittle down the degradation of the mesopore framework. The proposed methodology allows us to optimize MSNs regarding hydrolytic stability for targeted and controlled cargo release for drug delivery applications.

2. Experimental Section

2.1 Materials:

Hexadecyltrimethylammonium bromide (CTAB, H5882), hexadecyltrimethylammonium chloride 25% in water (CTAC), tetraethyl orthosilicate (TEOS), (3-mercaptopropyl)trimethoxysilane (MPTMS), triethanolamine (TEOA), 1,3,5-Triisopropylbenzene (TIPB), HCl 37%, phosphate-buffered saline (PBS) tablets, and all other reagents were purchased from Sigma-Aldrich (Germany). Tetrapropyl orthosilicate (TPOS) was purchased from Alfa Aesar (UK). Sodium chloride (NaCl) was purchased from Fisher (Belgium). Gradient HPLC-grade water was used in all syntheses and dissolution experiments. 100 nm-polystyrene (PS) beads in a 2.5% (w/v) aqueous suspension were purchased from Polysciences Inc (USA).

2.2 Synthesis of large-pore MSNs (k-MSN$_x$):

Large-pore *k*-MSNs were synthesized using a modified protocol based on a previously reported method. [28]. Firstly, seed NPs were prepared. TEOA (0.70 g, 4.7 mmol) and CTAB (3.33 g, 9.14 mmol) were dissolved in 400 mL of water in a 500 mL round-bottomed flask. The mixture was stirred at 700 rpm for 1 hour at 80 °C using an olive-shaped magnetic stirring bar (40×20 mm). Then, TEOS (0.78 mL; 3.5 mmol) was added to the solution with stirring at 900 rpm, and the mixture reacted at 80 °C for 1 hour. The obtained colloidal suspension was slowly cooled to 33 °C with stirring. Secondly, the seed NPs were grown using the following seed-growth method. A pore-expanding agent, TIPB (0.109 mL, 0.218 mL, or 0.544 mL, equivalent to 0.45 mmol, 0.91 mmol, or 2.3 mmol, respectively), was added to a seed colloidal suspension (100 mL) in a beaker immersed in a water bath at 33 °C. Then, TPOS (0.580 mL, 2.0 mmol) was added. The colloidal suspension was stirred for 2 days at 33 °C. The addition of TPOS (0.580 mL, 2.0 mmol) was repeated with MPTMS (0 or 0.2 mmol, 0 or 10 mol% of Si atoms). The reaction was kept at 33 °C for 2 days under stirring. The suspension was cooled to room temperature by stirring. Finally, the resulting MSNs were centrifuged and washed with ethanol. The organic template was removed via acid extraction. The resulting MSNs were stirred overnight with 50 mL of a 9:1 mixture of ethanol (95%) and concentrated HCl (37%) at 60 °C in a 100 mL round-bottom flask. The template-free MSNs were separated by centrifugation (20 min, 41000 rcf, 4 ℃). Afterward, 3-fold washing cycles with ethanol, water, and ethanol were performed in centrifuge tubes for at least 30 min under sonication and centrifuged accordingly. Lastly, the as-prepared MSNs were dried overnight at 60 °C to yield a white powder. The samples were denoted as *k*-MSN$_x$ or *k*-MSN$_x$-SH (*x* indicates the amount of TIPB: 0, 0.2, 0.4, and 1.0 for 0 mL, 0.11 mL, 0.22 mL, or 0.54 mL of TIPB, respectively).

Comparable large-pore MSNs, denoted as b-MSNs, were prepared under basic pH conditions.[29] To this purpose, TEOA (0.10 g, 0.67 mmol) was added to 20 mL of water in a 50 mL round bottom flask. Concomitantly, 25% aqueous CTAC solution (2.0 g, 1.6 mmol) and TIPB (3.0 mL, 1.2 mmol) were dissolved, and the mixture was stirred at 700 rpm with an olive-type stir bar (5×15 mm). The solution

was heated up to 90 °C and kept for 1 hour. TEOS (2.0 mL, 9.0 mmol) was then added dropwise over 30 s. The solution was stirred at this temperature for 4 hours at 700 rpm. The resulting MSNs were collected and extracted from the reaction medium described above.

2.3 Degradation experiments:

A 0.3 mg/mL suspension of NPs was prepared by sonicating a mixture of MSNs (3.0 mg) and water (10 mL) for 3 to 5 minutes until the DLS cumulant size was below 200 nm. This mixture (1.0 mL) was added to a medium at 37 °C (2.0 mL) to reach a 0.1 mg·mL^{-1} concentration in NPs. The medium was either pure water or water (1.7 mL) with a ten-times concentrated solution (300 µL) of PBS, NaCl, or ethanol to reach the desired medium concentration. The suspension was kept at 37 °C and monitored by standard or confocal DLS or by SEM or TEM by taking aliquots (3 µL), diluting them with ethanol (300 µL), and then drying them on a piece of silicon wafer or copper grid for SEM or TEM, respectively.

2.4 Characterization:

SEM micrographs were obtained at 3.0 kV on a Zeiss Gemini ULTRA plus electron microscope. Micrographs of initial MSNs were obtained after air-drying a 3 µL drop of an ethanol suspension on a piece of a silicon wafer. Mean particle sizes and standard deviations were obtained from the SEM micrographs by measuring the dimensions of at least 100 particles. For transmission electron microscopy (TEM), ethanolic suspensions were dropped on a Cu grid covered with holey carbon and dried for several hours. Low- to high-magnification TEM imaging was carried out using a JEOL NEOARM operating at 200 kV and equipped with a sensitive Gatan One View 4K CMOS camera. Experimental conditions were optimized for pore visualization (contrast aperture, defocus).

Thermogravimetric analyses (TGA) and differential thermal analyses (DTA) were carried out on a SETARAM TAG 16 instrument, using 8-10 mg samples within an alumina crucible under an oxygen flow with a heating rate of 10 °C·min^{-1}. These TGA and DTA characterizations were coupled to mass spectrometry of gas exhausts using an HIDEN analytical apparatus (QGA-HAL201-RC).

DLS measurements were conducted at a scattering angle of 173° on a VASCO Kin™ instrument equipped with a homemade heating jacket at 37 °C (Figure S1). DLS measurements in a very small observation volume ($\sim fL$) were carried out on a homemade set-up consisting of a confocal microscope coupled with a photon correlator (Figure S2) [30]. Briefly, the sample is illuminated by an incident green laser ($\lambda = 532$ nm) through a ×60 water-immersion objective of numerical aperture $\mathrm{NA} = 1.22$. The elastic backscattered light is collected by the same objective and spatially filtered by a 50 m diameter pinhole placed in the confocal plane to limit the size of the observation volume. Normalized intensity autocorrelation functions (ACFs) are derived from the time-dependent intensities recorded using a NI-6602 National Instrument card. The analysis of the data is explained in the Supporting Material.

Nitrogen (N_2)-sorption measurements were performed on a Micromeritics Tristar 3000 apparatus at − 196 °C. Prior to the measurement, template-subtracted samples were degassed for 12 h at 80 °C under vacuum, 10^{-5} Torr. Langmuir-specific surface area calculations were carried out using the BET model within the range of $0.05 < p/p^0 < 0.25$, with a cross-sectional area of 0.162 nm^2 assigned for the adsorbed nitrogen molecules. The pore size from the adsorption branch was calculated using the BJH method.

^{29}Si-CP-MAS solid-state NMR spectra were recorded on a Varian VNMRS400 spectrometer at 79.41 MHz at a spinning rate of 6.0 kHz.

3. Results and discussion

3.1 Synthesis and characterization of k-MSN$_x$ and k-MSN$_x$-SH

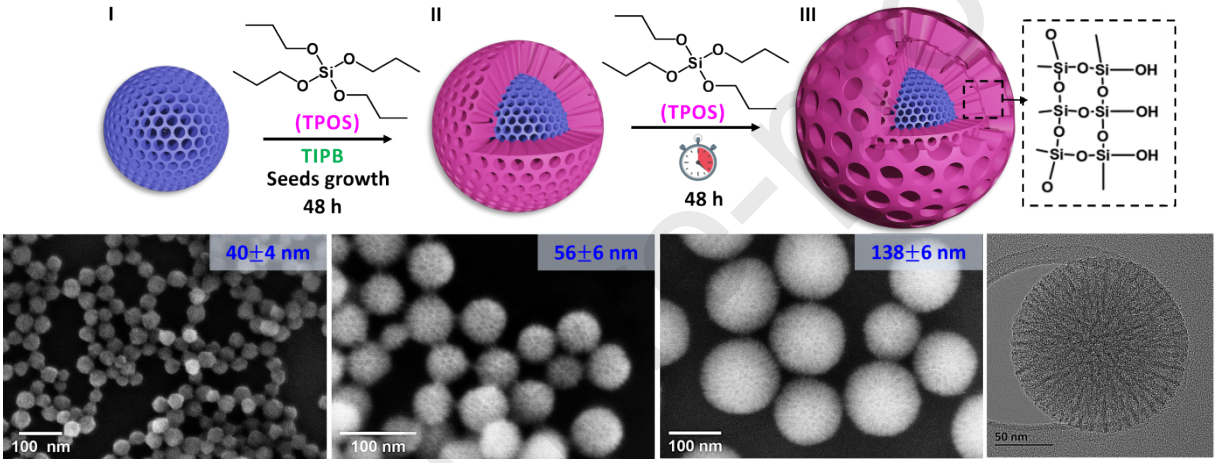

Figure 1. Top: schematic illustration of the preparation of monodisperse MSNs step-by-step with controlled particle and pore sizes for x = 1.0, where the SiO_2 shell is represented by (**o**) color. Bottom: SEM characterization of each step in the threefold growth process. The insert shows a TEM micrograph of the as-prepared MSN in the final step.

Monodisperse MSNs with controlled particle and pore sizes were obtained by preparing size-controlled seed MSNs, followed by the growth of the seeds by the addition of TPOS with TIPB as a pore-expanding agent (Figure 1). This growth method was adapted from a previously reported synthesis procedure.[28] Seed MSNs of 40 ± 4 nm were obtained as a colloidal suspension after the first step, with a hydrodynamic diameter of 65 nm. This indicates that most seed MSNs are present as individual and uniform NPs (Figure S3). From these initial seed MSNs, a second and third layer of silica with tunable porosities was grown using CTAB as a soft template, TIPB as a pore-expending agent, and TPOS as a silica source. TPOS is essential as its slower hydrolysis kinetics compared with the commonly used precursor TEOS enable a low supersaturation of hydrolyzed silicates. This prevents the formation of new nuclei that favor the growth around the as-prepared seeds. As mentioned earlier, each step during the process can be monitored by SEM, with an increase in particle size from 40 ± 4 nm to 56 ± 6 and up to 138 ± 6 nm (Figure 1).

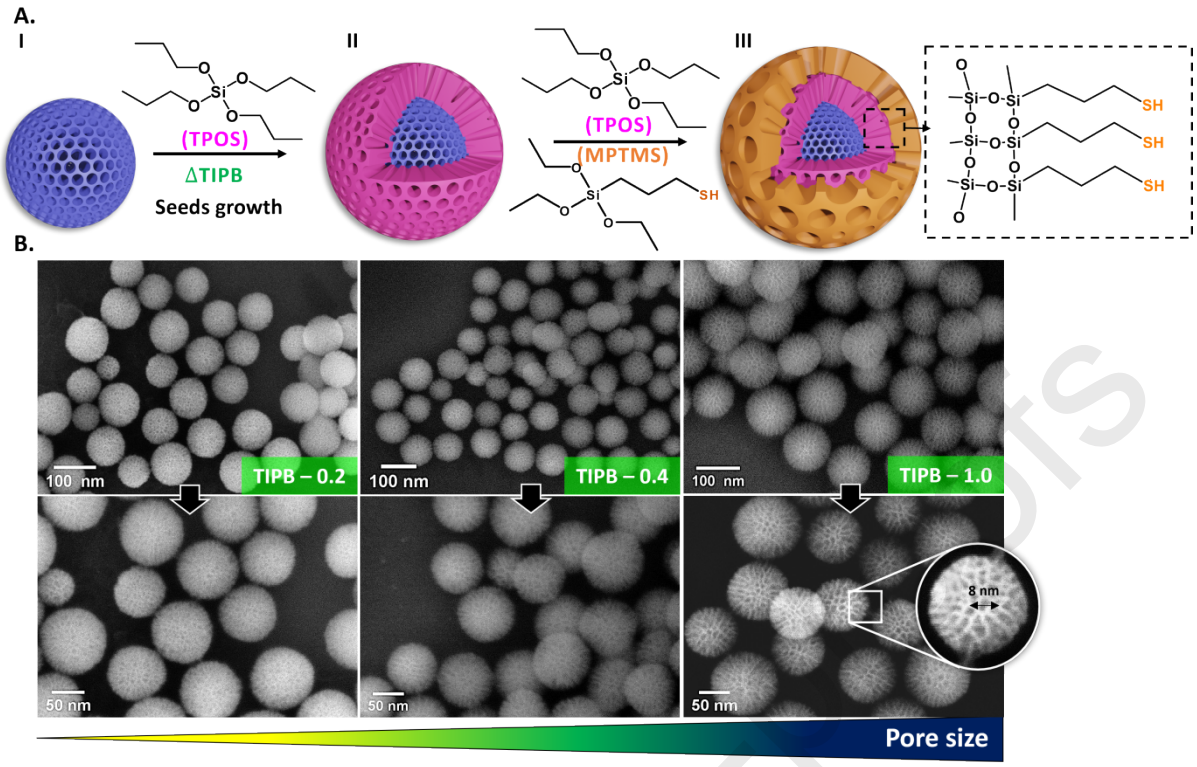

Figure 2. A. Illustration of the step-by-step growth process and the site-selective functionalization of large-pore MSN surface. **B.** SEM micrographs of *k*-MSN$_x$-SH synthesized with 10 mol% MPTMS and different amounts of TIPB as swelling agent where x = 0.2, 0.4, or 1.0.

Interestingly, this strategy can incorporate functionalities by a delayed co-condensation on the outer particle shell only when a functional organo(trialkoxy)silane is added to TPOS during the last growth step. This approach allowed us to grow monodisperse large-pore MSNs with a tunable number of functionalities. Therefore, we implemented this method to introduce functional mercaptopropyl moieties (-(CH$_2$)$_3$-SH, 10 mol % of Si atoms in the second growth step) in the outer shell of the particle. The as-prepared samples were denoted as *k*-MSN*x*-SH. TGA analysis (Figure S4) evidenced the successful incorporation of the mercaptopropyl functions, whose precise location cannot be entirely ascertained. However, due to the co-condensation during the last step of the synthesis, this approach inherently forces the implementation of functionalities on the outer shell. Indeed, the functionalization of MSNs is widely explored in drug delivery applications where functional groups attached to the periphery of the particles are used for the further coupling guest molecules.[31] The versatility of our approach is further demonstrated by the fact that the mesoporosity of the final material can be tailored depending on the amount of TIPB used during the last step. This flexibility allows for the creation of large pores of up to 8.0 nm, as inferred by SEM micrographs (Figure 2). To gain more insight into the porosity of both *k*-MSN and *k*-MSN-SH, N$_2$-sorption measurements were performed.

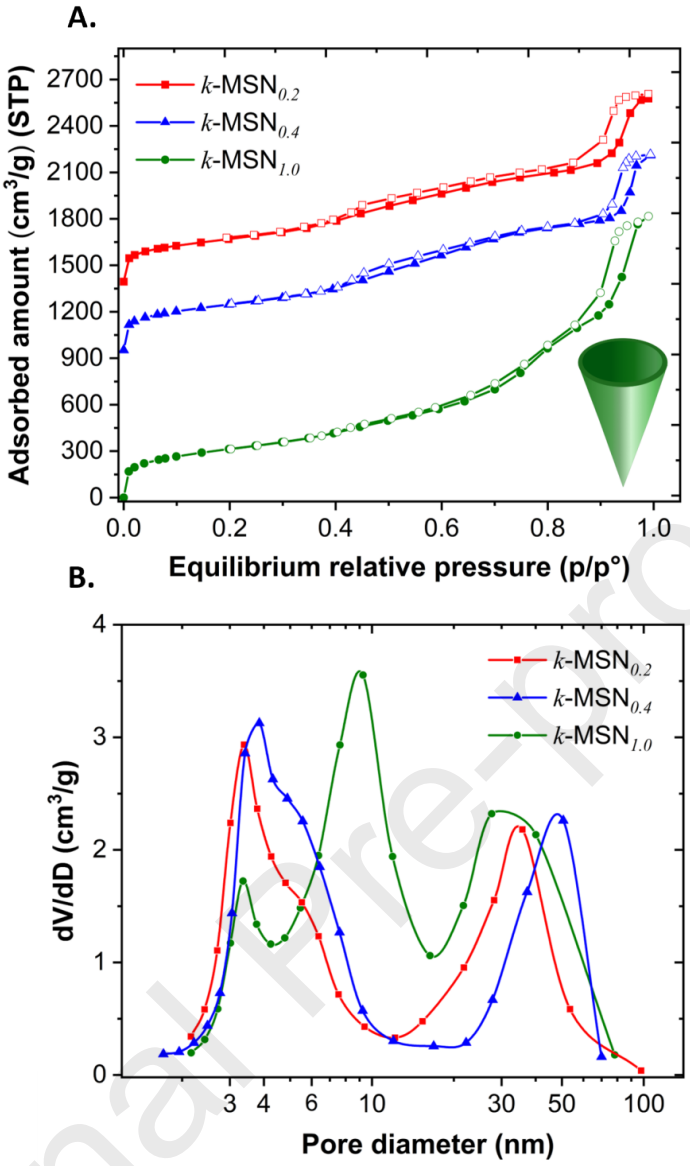

Figure 3. A. N_2-sorption isotherms and **B.** Pore size distribution obtained from the adsorption branches of the sorption isotherms using the BJH model. The insert shows the characteristic conical pore structure of large-pore *k*-MSN$_x$. Isotherms of *k*-MSN$_{0.4}$ and *k*-MSN$_{0.2}$ are offset by 900 and 1300 $cm^3 \cdot g^{-1}$, respectively.

Material	Specific surface area ($m^2 \cdot g^{-1}$)	Small pores 3.2 nm < D_p < 3.5 nm		Medium pores 5 nm < D_p < 15 nm	
		Vp / $cm^3.g^{-1}$	%	Vp / $cm^3.g^{-1}$	%
k-MSN$_{0.2}$	1009	251	58	178	42
k-MSN$_{0.4}$	1031	265	53	229	47
k-MSN$_{1.0}$	1114	183	23	600	77
k-MSN$_{1.0}$-SH	1108	180	29	438	71
k-MSN$_{0.2}$-SH	1032	111	40	169	60
k-MSN$_{0.4}$-SH	1470	160	29	400	71
b-MSN	452	3 nm < D_p < 8 nm		Vp = 138 / $cm^3.g^{-1}$	

Table 1. Textural properties of the materials. Definition of the different mesoporosities and contributions to the different mesopore volumes after exclusion of the largest mesopores, in absolute values and percentage related to the capillary condensation processes.

The N_2-sorption isotherms of *k*-MSN$_x$ particles, as shown in Figure 3, share similar features. Their specific surface areas, as detailed in Table 1, are in the same range. The application of the *t*-plot method to the three sorption isotherms revealed no microporosity. Furthermore, all *k*-MSN$_x$ samples were found to be mesoporous materials, as shown by the presence of three sub-steps during the sorption process. The precise location deduced using the first derivative of the isotherms (Figure S5) is consistent with the pore size distributions (Figure 3B). These distributions exhibit three different mesopore populations: the largest pores can typically be attributed to interparticular voids between NPs, which are not relevant in the frame of this study. We therefore discuss the relative importance of the small and intermediate pore populations at the mean values of *ca*. 3-5 nm and 5-15 nm, respectively. Interestingly, the mesopores filling that appears at the relative pressure around $0.2 < p/p^0 < 0.8$ is reversible for the two populations of pores, which strongly suggests that the largest inner mesopores (5-15 nm) exhibit a conical shape.[32] The conical mesopore channels can also be observed in the TEM micrographs (Figure 4 and S6). In addition, the proportion of the small pores to the total pore volume was estimated (Table 1). The different mesopore volumes were calculated by the first derivative of the total capillary condensation, taking the adsorbed amount at saturation, where the largest pores are filled at $p/p^0 = 0.9$ (Figure S5). Overall, the contribution of the largest pores to the total inner pore volume increased from *k*-MSN$_{0.2}$ to *k*-MSN$_{1.0}$. These mesopores appear to be generated at the expense of the smallest mesopores with sizes around 3 nm. This observation is highlighted by the volumic fraction of small mesopores, which is only 23 % in the case of *k*-MSN$_{1.0}$ and above 53 % in the case of lower TIPB contents, *k*-MSN$_{0.2}$ and *k*-MSN$_{0.4}$. Focusing on the smallest mesopores, their pore diameters are similar for all *k*-MSN$_x$ samples (3.2 – 3.5 nm, Figure 3B and Table 1). These small mesopores likely result from the initial structure of the mesoporous seeds (see Figure 1), where CTAB is used as a template. The effect of the addition of TIPB on the growth of the mesostructured phase is noticeable for the intermediate

pore sizes (between 5.0 – 15 nm), low content of TIPB leading to small mesopores (*k*-MSN$_{0.2}$ and *k*-MSN$_{0.4}$: 5 nm – 8 nm) whereas a high content leads to a significant enlargement of the pores (*k*-MSN$_{1.0}$: 6 nm – 15 nm). This result confirms the successful expansion of the mesoporous framework with an increase of TIPB content while keeping monodispersity in agreement with SEM observations.

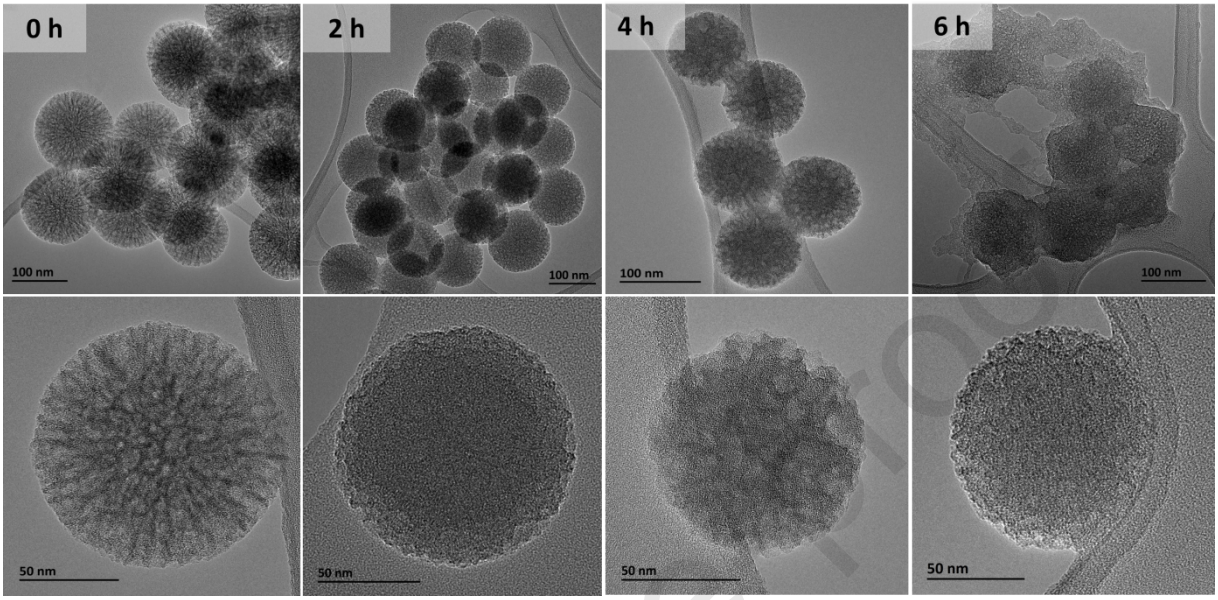

Figure 4. Top: TEM micrographs of MSNs at different incubation times in water at 37 °C. Bottom: Representative micrographs taken at similar magnification show the evolution of the porosity from conical to enlarged (swollen) pore structure.

Compared to the parent siliceous materials *k*-MSN$_x$, *k*-MSN$_x$-SH display similar textural properties, as suggested by N_2-sorption (Figure S7 and Figure S8). The specific surface areas are notably close (1114 and 1107 $m^2 \cdot g^{-1}$ for *k*-MSN$_{1.0}$ and *k*-MSN$_{1.0}$-SH, respectively). The main difference is related to the total pore volume lowered upon the functionalization with mercaptopropyl groups. This decrease can be attributed to introducing mercaptopropyl moieties in the large mesopores during the last growth step, where the co-condensation occurs.

3.2 Morphological evolution upon incubation in water under the solubility limit

As-prepared large-pore MSNs and MSNs-SH exhibit excellent dispersibility and colloidal stability in ethanol and pure water. However, the hydrolytic stability of the *k*-MSNs was found to be concentration-dependent in pure water. By monitoring via SEM a 0.1 $mg \cdot mL^{-1}$ suspension of *k*-MSN$_{1.0}$, under the silica solubility limit, which is around 0.2 $mg \cdot mL^{-1}$ in pure water at physiological temperature [22], we found that the density of NPs on the SEM substrate quickly decreased with time, despite a standardized sampling protocol. At the same time, some particles underwent a pore structure change, evolving with time into MSNs with widened pore openings denoted as swollen MSNs (*s*-MSNs), along with the remaining unaffected particles with unnoticeable morphological changes (Figure 5). Notably, the proportion of *s*-MSNs increases over time at the expense of the starting MSNs. Interestingly, during the first 4 h, MSNs with precisely the same appearance and diameter as the initial ones can be observed

while the *s*-MSNs feature a similar diameter as the unaffected MSNs. Although some *s*-MSNs were visible at $t = 0$ h by SEM, it should be noted that the sample was prepared after suspending the *k*-MSN$_{1.0}$ in water by sonication for 5 min. Thus, the changes may be attributed to this initial treatment. When a similar sample preparation is conducted in ethanol, the MSNs remain intact, as inferred by TEM analysis (Figure S6). Importantly, no fragment of MSN or other morphological transitions were observed in the course of the degradation study. We further analyzed the residual NPs by TEM after incubation in water at 37 °C (Figure 4). It is noteworthy that the pores and, therefore, the particle walls seem altered after only 2 hours. When stirred in water at this low concentration, the remaining NPs showed a progressive loss of the conical pore structure and rougher particle morphology. By contrast, other studies have described a degradation pathway of non-functionalized MSNs in aqueous media driven by fragmentation or erosion of the particle's surface.[10] The evolution of the mesostructure to form *s*-MSNs may be attributed to a local dissolution-reprecipitation process, where silicates would dissolve and re-attach within the same NP.

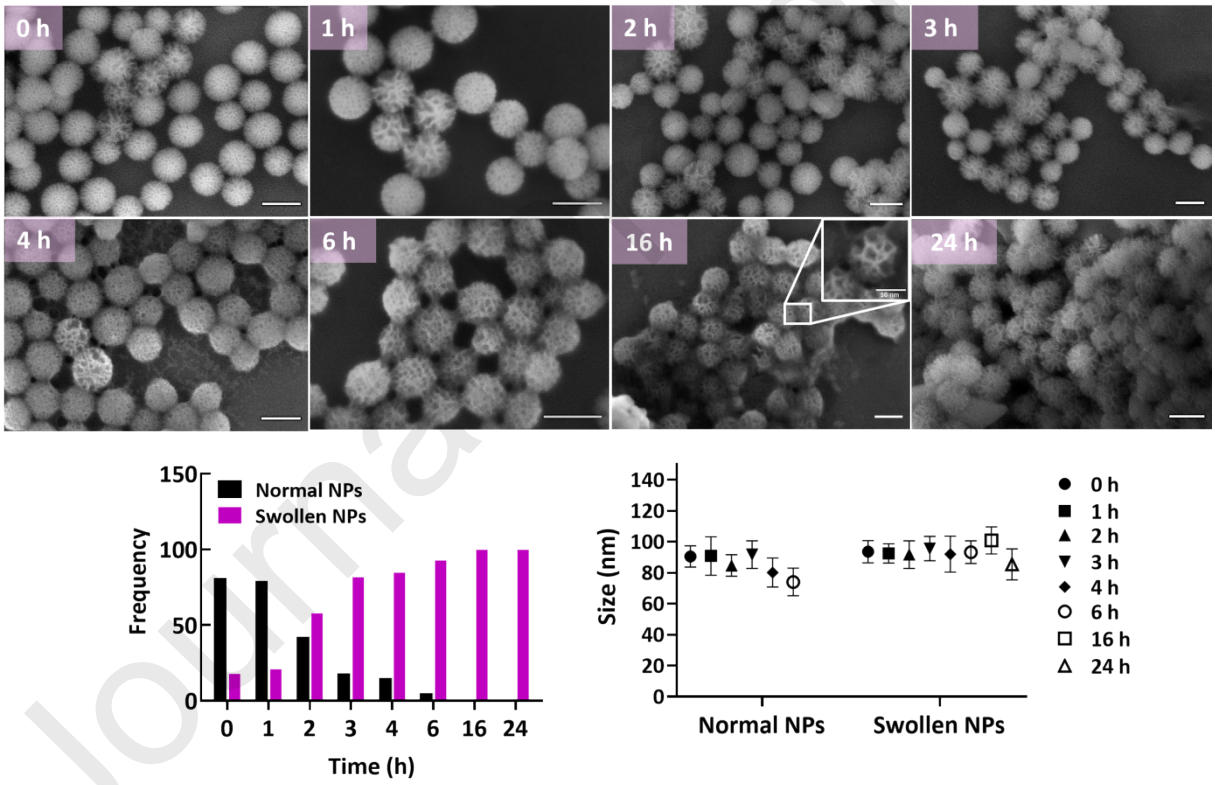

Figure 5. SEM micrographs and statistical analysis of the morphological evolution of siliceous and large-pore MSNs after incubation in pure water at 37 °C. Particle sizes are given as mean ± SD and determined by SEM. Samples at 0 hours were taken after 5 min of sonication in water. All scalebars in SEM images are 100 nm.

The functionalization of MSNs was found to modify their degradation behavior. In contrast to the pure siliceous large-pore *k*-MSNs, *k*-MSN$_{1.0}$-SH, with similar porosity to their parent particles, present a slightly different dissolution profile. SEM studies revealed that *k*-MSN$_{1.0}$-SH are less prone to morphological changes, and the transition from *k*-MSN$_{1.0}$-SH to *s*-MSNs was less noticeable than for *k*-

$MSN_{1.0}$. Nonetheless, after 6 hours, the particle size becomes smaller, and more compact particles can be detected in solution after 16 hours, indicating an additional stage of dissolution, in which the last shell composed mainly of mercaptopropyl functionalities may be degraded first, leading to smaller particle of *ca.* 60 nm (Figure S9).

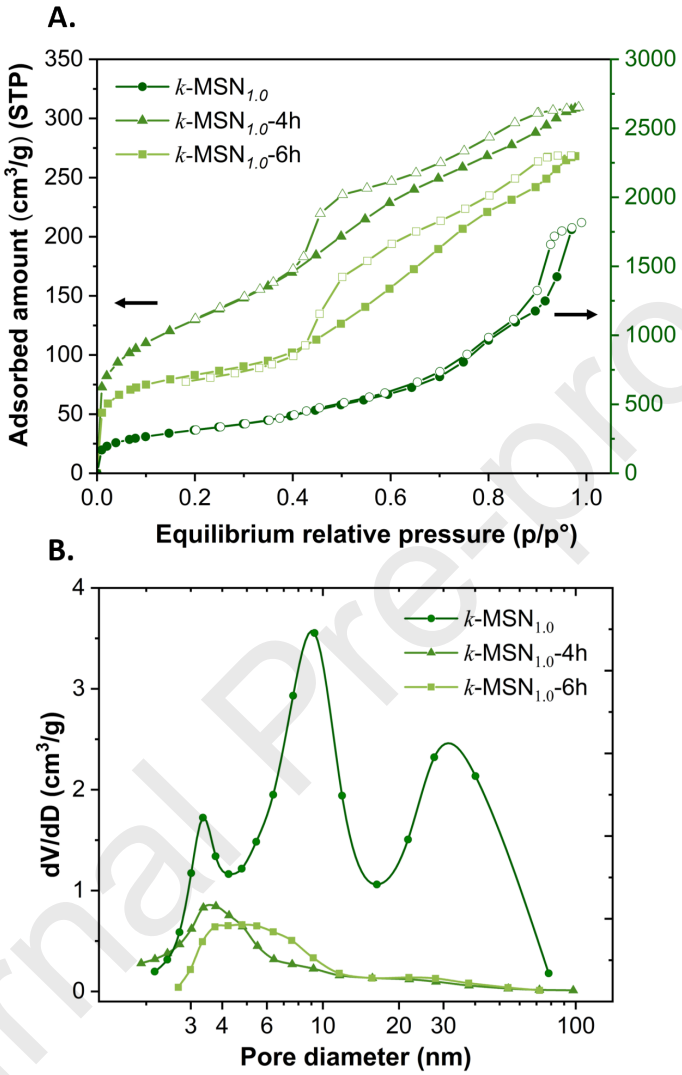

Figure 6. A. N_2-sorption isotherms performed on *k*-$MSN_{1.0}$ at different dissolution times; **B.** Pore size distribution obtained using the BJH model on the adsorption branches of the sorption isotherms.

The formed *s*-MSNs obtained after 4 and 6 hours of degradation of *k*-$MSN_{1.0}$ were further investigated by TEM and N_2 physisorption analysis after separating the solid residues from the supernatant by centrifugation, although in a meager yield. Despite the low amount of recovered material, N_2-sorption experiments could be performed in both cases, affording isotherms that are reliable in shape. However, an accurate determination of the surface area and pore volume is not possible due to the low precision of the weight. The N_2-sorption isotherms obtained for *k*-$MSN_{1.0}$-4h and *k*-$MSN_{1.0}$-6h are reported in Figure 6, along with those of the parent material *k*-$MSN_{1.0}$. The *k*-$MSN_{1.0}$-4h and *k*-$MSN_{1.0}$-6h differ in the smaller pore diameters region (Figure 6B and Figure S10) as *k*-$MSN_{1.0}$-6h has a broad population of

mesopores between 3.5 and 10 nm which is split into two populations in the case of *k*-MSN$_{1.0}$-4h. Importantly, hysteresis loops are observed for k-MSN$_{1.0}$-4h and k-MSN$_{1.0}$-6h, by contrast to the isotherms of the parent *k*-MSN$_{1.0}$. This indicates that interconnected pores are present after hydrolysis into *s*-MSNs, this observation being corroborated by TEM and SEM observations (Figures 4 and 5).

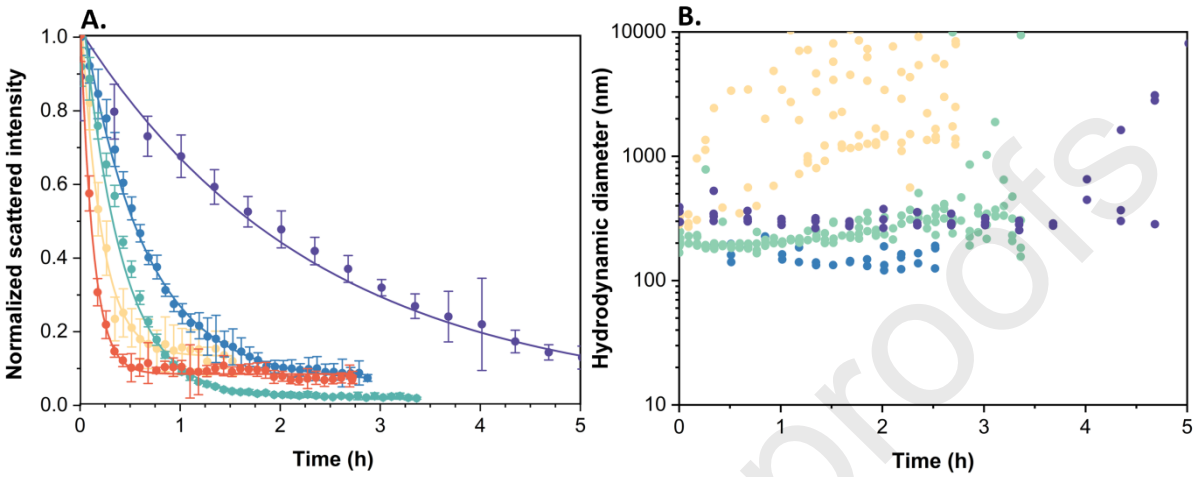

Figure 7. A. Scattered intensities measured as a function of incubation time with first-order exponential decay fit for a concentration of 0.1 mg·mL^{-1} at 37 °C; **B.** Evolution of the DLS diameter obtained with the cumulant fit. (blue) pure water; (yellow) PBS 1×; (green) PBS 0.1×; (orange) NaCl 137 mM; (purple) H_2O/EtOH 85/15 % v:v.

3.3 Monitoring of the hydrolytic process by DLS

To get insights into the mechanisms that lead to a low yield of *s*-MSNs during the aqueous incubation of the particles and to determine the kinetics of the process, we monitored *in situ* the colloidal stability of an aqueous suspension of large-pore *k*-MSN$_{1.0}$ at a concentration of 0.1 mg·mL^{-1} via standard DLS. For such a purpose, the optical DLS probe, which collects light backscattered at 173°, was located at its focal distance from the dissolution vial.[33] The vial was placed within a heating jacket to evaluate the kinetics of MSN degradation at a relevant temperature of 37 °C (Figure S1). The Rayleigh scattering intensities were monitored over several hours as a function of time, and intensity ACFs were recorded to determine the hydrodynamic diameter of the NPs. The NP size remained constant during acquisition (Figure 7). However, the mean scattered intensity averaged over 1 second decreased rapidly during the same period following an exponential decay law. It was verified that this decrease could not be ascribed to a sedimentation process or from the re-precipitation of silica, as the intensity did not change when the vials were shaken from time to time. To understand these observations, it should be noted that in the electrostatic limit,[34] the intensity scattered by N independent and identical spherical particles of diameter d at a space point M(r, θ) can be expressed as:

$$I(r,\theta) = Nd^6\sigma\frac{\pi^4}{8\lambda^4 r^2}(1 + cos^2\theta)I_0 \quad (1)$$

Where $\sigma = \left(\frac{m^2-1}{m^2+2}\right)$ with m the ratio of the refraction index of the particles to that of the solvent and I_0, corresponding to the incoming light intensity. At a fixed position of the detector, a decrease in the scattering intensity may thus correspond to a decay in N or/and in the size of particles d, or/and in the increase in their porosity such that σ tends to 0. The time-evolution of the scattered light, normalized by the intensity at the initial time $t = 0$, can thus be expressed as:

$$\frac{I(t)}{I(0)} \propto N(t)d(t)^6\sigma(t) \quad (2)$$

for which a mono-exponential decay is observed in the present case.

As mentioned above, standard DLS can determine an average diameter. However, this method does not provide information on the number of particles or their scattering efficiency, σ. Following the demonstration by Rigler *et al.* within the framework of fluorescence correlation spectroscopy[35] we know that a drastic reduction of the probing volume permits access to the concentration of the colloidal suspension. Furthermore, Qian *et al.* proposed a data processing method to assess the scattering efficiency in this same experimental framework.[36] Therefore, we conducted DLS experiments under a confocal microscope to explain the observed intensity decay unambiguously. For this, the temporal fluctuations of the scattered light were recorded during 10-second scans, each being repeated 5 to 10 times. Due to the low local concentration, the NPs are measured sequentially as they cross the observation volume, each crossing resulting in a scattering event that triggers a burst of intensity (Figure S2B). Intense bursts occur frequently at the beginning of the degradation process, but their number and intensity gradually diminish over time. This behavior can be due to the particles vanishing or losing their scattering efficiency. However, the formation of large aggregates can be ruled out as they would give rise to strong intensity bursts (as the scattering is in d^6) and ACFs with larger diffusion times that are not observed. To access quantitative results, a statistical analysis is performed to correlate these temporal fluctuations to the dynamic properties of the particles. The first step consists of deriving the ACF of the intensities (Figure S2C) for the first five hours and measuring the ACFs for a stable reference sample of polystyrene beads. Over time, the amplitudes of the ACFs measured on the *k*-MSN$_{1.0}$ colloidal suspension decrease significantly to the point of no longer being physical. By contrast, those measured on the reference sample are relatively stable, with minor fluctuations. These ACFs obey the following equation:

$$G(\tau) - 1 = \beta e^{-\frac{t}{\tau_c}} + \frac{c^2}{\langle N \rangle} \frac{1}{\left(1+\frac{t}{\tau_D}\right)\sqrt{1+\frac{t}{\omega^2\tau_D}}} \quad (3)$$

the first term is due to the time-dependent interferences of the electric field scattered by the different NPs, and the second term is related to the time-dependent local concentration of the colloids. [30,37] Both terms decay as a function of time with characteristic times: τ_c and τ_D, respectively. These terms

are proportional to the diameter of the NPs and are visible in Figure S2C. The vanishing of the ACFs is due, for the first term, to the disappearance of the interferences when the local concentration falls below 1. The second term also decreases with the local concentration despite the increase in the factor $(1/\langle N\rangle)$. This is due to the signal-to-noise ratio $(c = I_{NP}/I_T)$ where I_{NP} is the intensity scattered by the particles and I_T is the total measured light intensity concomitantly falls to zero as I_{NP} (proportional to *N*) tends to zero. To perform a quantitative analysis, the ACFs were fitted according to Eq. (3) to determine the characteristic times τ_c and τ_D and the value of $c^2/\langle N\rangle$. The term $0 \leq \beta \leq 1$ is the Siegert coefficient linked to the experimental geometry, which does not give information on the sample. [38] This is the same for the term ω which is the form factor of the observation volume and whose value is known from the calibration measurements. The hydrodynamic diameters of the MSNs were calculated from the characteristic times, while the value of $\langle N\rangle$ and the scattering efficiency σ were obtained following Qian's procedure.[36] The complete data analysis procedure is provided in the Supporting Information. The same procedure was applied to the reference sample of polystyrene to ensure that the observed effects could not be attributed to experimental artifacts.

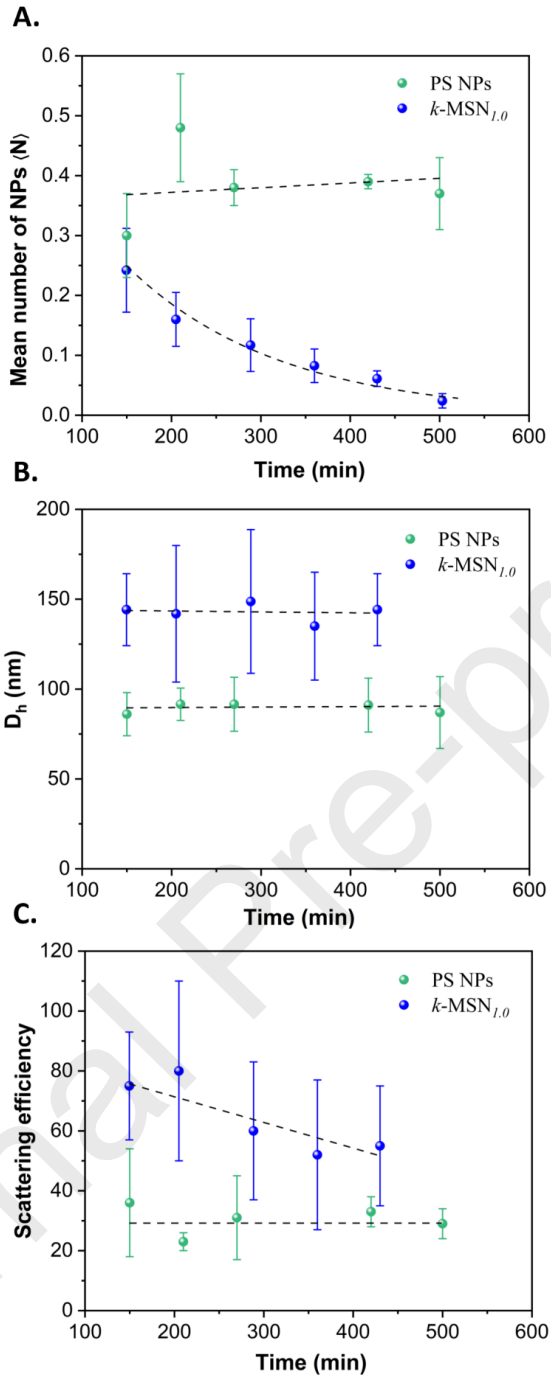

Figure 8. Confocal DLS dissolution studies on *k*-MSN$_{1.0}$ using a concentration of 0.1 mg·mL^{-1} at 37°C (blue) and on PS reference particles (green). **A.** The average number of NPs ⟨N⟩ in the confocal volume, **B.** Mean hydrodynamic diameter, $D_{h,}$ and **C.** Scattering efficiency per NP. The error bars correspond to the limit values obtained when repeating the measurements under the same conditions.

The obtained results from the confocal DLS analysis are presented in Figure 8. The reference sample of 100 nm-polystyrene beads exhibits the behavior expected for a stable colloidal solution and unchanging experimental conditions. Indeed, the constant value of the measured diameter indicates that the beads remain unaltered in size over time. Furthermore, the stability of the $\langle N \rangle$ values and the scattering

efficiency σI_0 confirms that the confocal volume and the incident intensity remained constant throughout the experiments. In the case of the *k*-MSN$_{1.0}$ colloid, the measured hydrodynamic diameters remained steady over the experiment time, as previously observed in standard DLS. Conversely, the mean number of NPs presents an exponential time-decay of the form $\langle N(t)\rangle = \langle N_0\rangle e^{-t/\tau}$, with $\langle N_0\rangle = 0.6$ and $\tau = 72$ min, corresponding to a half-life of 120 min. Finally, the scattering efficiency (σ) was relatively stable during the first few hours and decreased slightly after a few hours. The particles remaining in the solution may thus undergo an increase in porosity, which does not play a significant role in the DLS experiments.

These DLS experiments under a confocal microscope thus unambiguously attribute the exponential decay of the scattered intensity in the *k*-MSN$_{1.0}$ colloid observed by standard DLS to the evolution of the concentration in NPs. The sharp decrease in particle concentration is consistent with the low material yields obtained after 4 and 6 hours of incubation. Furthermore, it should be noted that no ACF with a characteristic time smaller than the ones observed for the initial MSN was detected. This agrees with the presence of only two kinds of NPs with similar diameters observed by SEM and TEM.

3.4 Influence of the composition and medium on the dissolution kinetics

Sample	Conditions	τ (h)	*k'* (g·m^{-2}·h^{-1})
k-MSN$_{1.0}$	37 °C, H_2O, 0.3 mg·mL^{-1}	4.27±0.11	2.1 10^{-4}
k-MSN$_{1.0}$	37 °C, H_2O, 0.2 mg·mL^{-1}	1.98±0.04	4.5 10^{-4}
k-MSN$_{1.0}$	37 °C, H_2O, 0.1 mg·mL^{-1}	0.76±0.02	1.2 10^{-3}
k-MSN$_{1.0}$	37 °C, H_2O, 0.05 mg·mL^{-1}	0.68±0.02	1.3 10^{-3}
k-MSN$_{1.0}$	37 °C, PBS 1×, 0.1 mg·mL^{-1}	0.19±0.02	4.7 10^{-3}
k-MSN$_{1.0}$	37 °C, NaCl 137 mM, 0.1 mg·mL^{-1}	0.13±0.01	6.9 10^{-3}
k-MSN$_{1.0}$	37 °C, PBS 0.1 ×, 0.1 mg·mL^{-1}	0.39±0.01	2.3 10^{-3}
k-MSN$_{1.0}$	37 °C, H_2O/EtOH 15%, 0.1 mg·mL^{-1}	2.36±0.06	3.8 10^{-4}
k-MSN$_{1.0}$	27 °C, PBS 1×, 0.1 mg·mL^{-1}	0.75±0.06	1.2 10^{-3}
k-MSN$_{1.0}$-SH	37 °C, H_2O, 0.1 mg·mL^{-1}	13.4±0.2	6.7 10^{-5}
k-MSN$_{0.4}$	37 °C, H_2O, 0.1 mg·mL^{-1}	1.5±0.1	6.5 10^{-4}
b-MSN$_{1.0}$	37 °C, H_2O, 0.1 mg·mL^{-1}	65±4	3.4 10^{-5}
b-MSN$_{1.0}$	37 °C, PBS 1×, 0.1 mg·mL^{-1}	1.92±0.09	1.2 10^{-3}

Table 2: Lifetimes τ obtained for the hydrolysis of large-pore MSNs under various conditions according to a monoexponential decay $I = I_0\, e^{\frac{-t}{\tau}}$. *k'* is the corresponding rate constant normalized by the specific surface area.

The functionalization of MSNs plays a crucial role in drug delivery application, but it also influences the interaction between the silica NP surface and the media. It can, consequently, lead to different degradation rates. This process can be boosted or slowed down depending on the surface modification. To investigate if the mercaptopropyl functionalities linked to the outer particle surface of large-pore MSNs influence the dissolution pathway observed with pure siliceous MSNs, we performed DLS studies with 10 mol % MSNs-SH (Table 2). Standard DLS evidences a monoexponential decay with a much

longer time constant (13 hours *vs* 0.76 hours for *k*-MSN$_{1.0}$-SH and *k*-MSN$_{1.0}$, respectively). By confocal DLS, no significant change in concentration and diameter could be detected over the 8-hour-long experiment, notably because of significant experimental uncertainties (Figure S11).

Experiments varying the particle concentrations and media compositions were performed using pure siliceous large-pore *k*-MSN$_{1.0}$ (Table 2 and Figure S12). The results highlight the crucial role of the particle concentration in the silica dissolution. Notably, highly diluted conditions of 0.1 mg·mL^{-1} led to a faster hydrolysis rate, a phenomenon previously observed for dense, 44 nm-sized Stöber silica NPs.[22] Large-pore MSNs were found to be fully dispersed in pure water at 37 °C for an initial concentration of 0.3 mg·mL^{-1}. This concentration was also found to be the upper limit of the dispersibility of *k*-MSN$_{1.0}$, thus the DLS monitoring protocol cannot be applied above this concentration. The 0.3 mg·mL^{-1} concentration is also above the reported silica solubility limit for dense silica nanoparticles. [22] Thus, complete hydrolysis into silicic acid should not be possible, favoring dissolution-reprecipitation processes. However, total solubilization happened, evidenced by the scattering loss, and was checked after shaking the sample. A higher energy for the amorphous large pore silica may be the origin of this higher solubility. [39] Dissolution rates were particularly elevated in PBS 1× (Figure 7 and Table 2). This effect is attributed to an elevated sodium chloride (NaCl) concentration, with similar hydrolysis rates observed for PBS or pure NaCl solution at the same sodium concentration. This effect may be attributed to the electrophilic activation of the surface silanols by sodium atoms to make the silicon atom more electrophilic, thus making it more prone to nucleophilic attack by the surrounding water molecules. Decreasing the PBS concentration by a factor of 10 reduced the dissolution rate by a factor of 2. We also addressed the effect of temperature on the hydrolysis in PBS 1×, with a 4-fold decrease of the hydrolysis rate when the temperature was diminished from 37 to 27 °C. When the medium was changed from pure water to an 85:15 v/v water: ethanol mixture, the reaction rate also strongly decreased by a factor of 3. Such a modification may be easily implemented to functionalize MSNs with biomolecules such as DNA or antibodies, where the MSN particles must be incubated in an aqueous medium for a long time to ensure a successful coupling. These findings equip us with means for a rational design of large-pore MSN properties towards their applicability in biological media when used as nanocarriers of biomolecules.

To get a comprehensive view of the degradation of large-pore MSNs, we include dissolution studies with pure siliceous MSNs of comparable size and pore structure prepared following a slightly different synthesis route at $pH = 8$. We adopted a protocol developed by the group of T. Bein to obtain particles of comparable structure, including TIPB as a swelling agent.[29] These particles were named *b*-MSNs. The synthesis conditions and the pH during the NP preparation influence the silica framework connectivity, which might also affect the dissolution outcome of large-pore MSNs. This method then involves the preparation of a single generation MSNs of *ca.* 60 nm. Notably, the *b*-MSNs prepared at basic pH showed a pronounced long-term resistance against hydrolysis, with a half-life in normal PBS

of 1.3 hours *vs* 0.13 hours for *b*-MSN and *k*-MSN$_{1.0}$, respectively (Figure S13 and Table 2). The same trend was found in pure water (half-lives of 45 and 0.5 hours, respectively). This trend cannot only be attributed to the specific surface areas of the materials, as the dissolution rates normalized by the surface area are still 4 and 35 times higher for *k*-MSNs in PBS and pure water, respectively (Table 2). Interestingly, a transition from *b*-MSNs to *s*-MSNs was also evidenced by SEM (Figure S14), though on a much longer timeframe (days *vs* hours). The textural properties of both materials are close (Figure S15), with a similar shape for the isotherms. However, the adsorbed amounts are lower for *b*-MSNs in the monolayer-multilayer region and during capillary condensation stages. The consequences are lower specific surface area and pore volume, as can be found in Table 1. Additionally, some differences in the pore size distributions can be found when focusing on the smaller pore sizes. Indeed, *k*-MSN$_{1.0}$ exhibits mesopores diameters located around 8 nm. These mesopores are downshifted to 4 nm in the case of *b*-MSNs. The pore volume is significantly decreased for *b*-MSNs, with only 0.5 $cm^3 \cdot g^{-1}$ at saturation $(p/p^0 = 0.85)$ compared to 1.7 $cm^3 \cdot g^{-1}$ for the similar *k*-MSN sample. Moreover, ^{29}Si NMR revealed that the degree of connectivity of the silica framework within these MSNs is higher for *b*-MSNs, with a more significant proportion of Q^4 sites than for other MSNs (Figure S16 and Table S1), at the expense of the less condensed Q^2 sites. Thus, *b*-MSNs feature fewer pores per particle, with thicker and more condensed silica walls than the studied *k*-MSNs. This high kinetic stability against hydrolysis at low concentrations was also reported by Möller and Bein in a series of MSNs prepared with varied condensation degrees at silicon.[18]

3.5 Mechanistic proposal for the degradation of large-pore mesoporous silica

All these observations suggest a novel dissolution mechanism where MSNs do not degrade simultaneously, as intact NPs are encountered by SEM over an extended period, whereas their concentration decreases rapidly. The MSN samples should thus be viewed as a population of NPs with a small diversity that does not follow the same trend over time. In the first place, large-pore MSNs are stochastically weakened and then quickly hydrolyzed into molecular or small fragments, as depicted in Figure 9. The fragments might exhibit such a short lifetime that they are not detectable under *in situ* confocal DLS experiments or by SEM. *s*-MSNs are putative intermediates in the degradation process. Indeed, the observation by SEM and TEM of *s*-MSNs with interconnected pores from an initial population of very similar NPs with conical pores may suggest that MSNs are first transformed into *s*-MSNs before being fully hydrolyzed. Thus, the MSNs with initially unconnected conical pores would transform during this transformation into *s*-MSNs, which display a modified porosity with larger interconnected pores. These *s*-MSNs would then hydrolyze into molecular species, as no fragments could be detected. The presence of intact NPs even after most NPs have disappeared is particularly counter-intuitive, as most reports suggest that all NPs degrade similarly at the same time. Electron microscopy techniques often evidence small fragments or modified NPs.[10,17] However, it is important to note that in all relevant MSN dissolution studies, the evolution of the degradation was

checked by ICP or the silico-molybdenum assay. [11,18,22] These methods, while helpful, do not allow to follow the concentration of NPs as we have uniquely performed in this study using both standard and confocal-volume DLS.

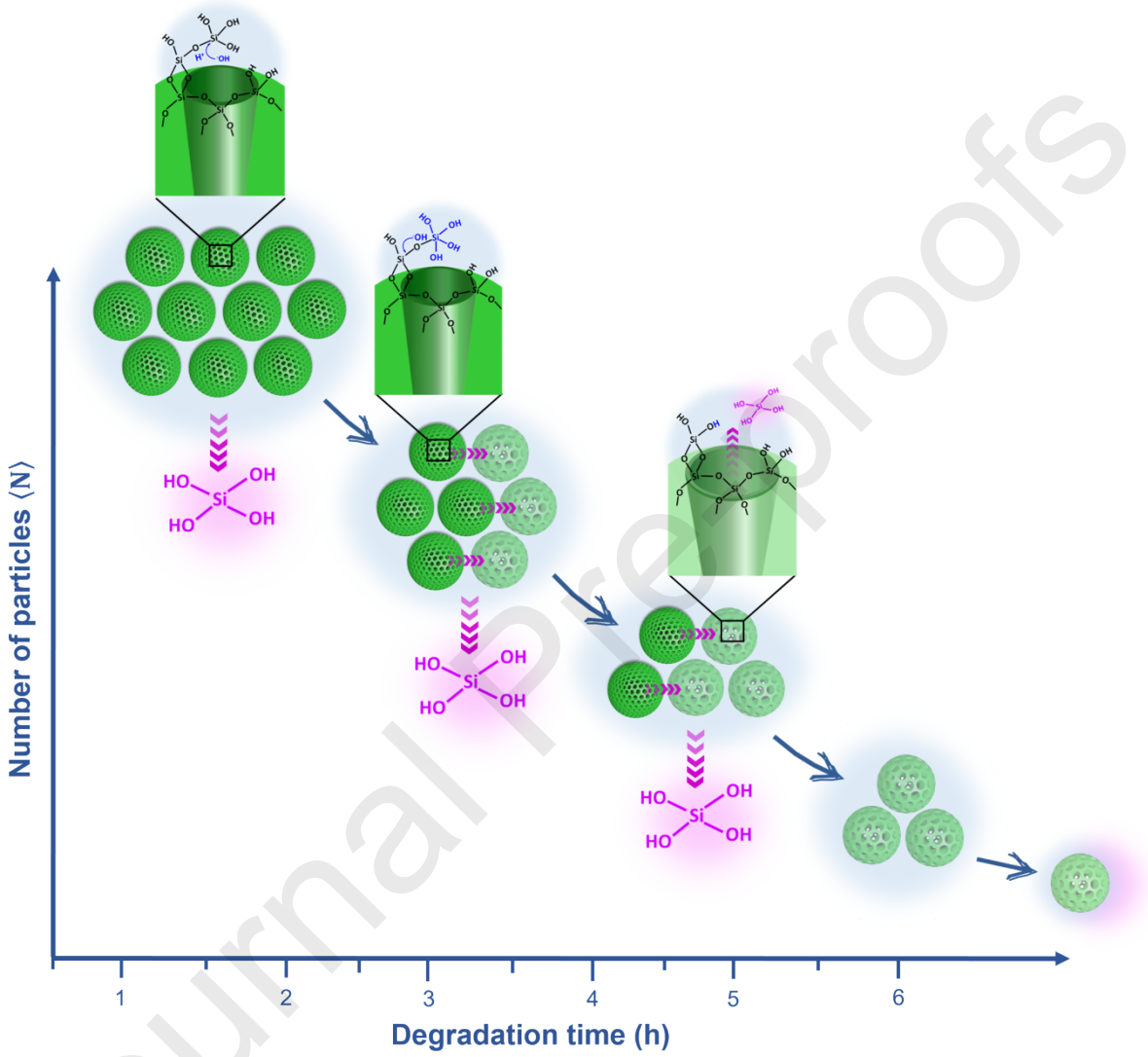

Figure 9. Proposed mechanism for the dissolution of *k*-MSNs or *b*-MSNs: from a population of nanoparticles with a small diversity, the first hydrolysis reactions fragilize some nanoparticles, which incidentally become much more fragile. Thus, they either directly hydrolyze into unobservable silicic acid or small oligomers or transition to form *s*-MSNs with interconnected pores. Unaffected MSNs can hence be observed over an extended time, while the concentration of nanoparticles has yet drastically decreased.

Conclusions

In this study, we investigated the hydrolysis of mesoporous silica nanoparticles with large conical pores using dynamic light scattering techniques and electron microscopies for various types of nanoparticles.

We prepared core-shell-shell architectures with a mesoporous silica core, covered with an inner shell of pure siliceous mesoporous silica with conical pores and an outer layer of mercaptopropyl-functionalized mesoporous silica. These nanoparticles form remarkably stable colloids in water or ethanol, which allowed dynamic light scattering studies at low concentrations. Unexpectedly, we found out that the populations of large-pore mesoporous silica nanoparticles do not dissolve homogeneously by reducing their size or fragmenting into smaller particles, as usually inferred or described in other studies. Instead, we observed by conventional dynamic light scattering and confirmed by dynamic light scattering under a confocal microscope that the number of nanoparticles decreases following a monoexponential decay law. Moreover, swollen nanoparticles with interconnected pores can be observed. These swollen mesoporous silica nanoparticles are putative intermediates in the dissolution process. Still, no other silica fragment could be followed by electron microscopies or detected by dynamic light scattering under a confocal microscope. This unprecedented heterogeneous mechanism [10,11] thus suggests that once fragilized by partial hydrolysis, the nanoparticles dissolve faster than the initial ones. Monitoring the scattered intensity is a very interesting technique to follow dissolution kinetics, though it can only be applied to nanoparticles forming stable colloids. The impact of environmental factors such as concentration, salinity, and temperature on the hydrolytic stability of *k*-MSNs could be easily quantified using such an approach. More work is ongoing to understand precisely the impact of functionalities on the dissolution kinetics of organo-functional *k*-MSNs with similar morphologies, while the imapct of proteins on the dissolution outcome certainly deserves to be considered.[17] As good control of the degradation kinetics is crucial for developing mesoporous silica nanoparticles towards nanomedicine, such investigations are of solid interest.

Acknowledgment

Christophe Bouchard (Institut Néel) is gratefully acknowledged for technical development. This study was financed by the Agence Nationale de la Recherche (ANR-20-CE09-0017). The TEM facility JEOL NEOARM at CNRS Institut Neel was co-financed by the European Union under the European Regional Development Fund (ERDF, contract n° RA0023813).

References

[1] Y. Feng, Z. Liao, M. Li, H. Zhang, T. Li, X. Qin, S. Li, C. Wu, F. You, X. Liao, L. Cai, H. Yang, Y. Liu, Mesoporous Silica Nanoparticles-Based Nanoplatforms: Basic Construction, Current State, and Emerging Applications in Anticancer Therapeutics, Adv. Healthc. Mater. 12 (2023) e2201884. https://doi.org/10.1002/adhm.202201884.

[2] N.B. Fernandes, Y. Nayak, S. Garg, U.Y. Nayak, Multifunctional engineered mesoporous silica/inorganic material hybrid nanoparticles: Theranostic perspectives, Coord. Chem. Rev. 478 (2023) 214977. https://doi.org/https://doi.org/10.1016/j.ccr.2022.214977.

[3] J.G. Croissant, K.S. Butler, J.I. Zink, C.J. Brinker, Synthetic amorphous silica nanoparticles: toxicity, biomedical and environmental implications, Nat. Rev. Mater. 5 (2020) 886–909. https://doi.org/10.1038/s41578-020-0230-0.

[4] R.R. Castillo, D. Lozano, B. González, M. Manzano, I. Izquierdo-Barba, M. Vallet-Regí, Advances in mesoporous silica nanoparticles for targeted stimuli-responsive drug delivery: an update, Expert Opin. Drug Deliv. 16 (2019) 415–439. https://doi.org/10.1080/17425247.2019.1598375.

[5] K. Möller, T. Bein, Talented mesoporous silica nanoparticles, Chem. Mater. 29 (2017) 371–388. https://doi.org/10.1021/acs.chemmater.6b03629.

[6] C. Tao, Y. Zhu, Y. Xu, M. Zhu, H. Morita, N. Hanagata, Mesoporous silica nanoparticles for enhancing the delivery efficiency of immunostimulatory DNA drugs, Dalt. Trans. 43 (2014) 5142–5150. https://doi.org/10.1039/C3DT53433B.

[7] G. V Deodhar, M.L. Adams, B.G. Trewyn, Controlled release and intracellular protein delivery from mesoporous silica nanoparticles, Biotechnol. J. 12 (2017) 1600408. https://doi.org/https://doi.org/10.1002/biot.201600408.

[8] M.M. Abeer, P. Rewatkar, Z. Qu, M. Talekar, F. Kleitz, R. Schmid, M. Lindén, T. Kumeria, A. Popat, Silica nanoparticles: A promising platform for enhanced oral delivery of macromolecules, J. Control. Release. 326 (2020) 544–555. https://doi.org/https://doi.org/10.1016/j.jconrel.2020.07.021.

[9] N. Knežević, J.O. Durand, Large pore mesoporous silica nanomaterials for application in the delivery of biomolecules, Nanoscale. 7 (2015) 2199–2209. https://doi.org/10.1039/c4nr06114d.

[10] A. da Cruz Schneid, L.J.C. Albuquerque, G.B. Mondo, M. Ceolin, A.S. Picco, M.B. Cardoso, Colloidal stability and degradability of silica nanoparticles in biological fluids: a review, J. Sol-Gel Sci. Technol. 102 (2022) 41–62. https://doi.org/10.1007/s10971-021-05695-8.

[11] J.G. Croissant, Y. Fatieiev, N.M. Khashab, Degradability, and Clearance of Silicon, Organosilica, Silsesquioxane, Silica Mixed Oxide, and Mesoporous Silica Nanoparticles, Adv. Mater. 29 (2017) 1604634. https://doi.org/10.1002/adma.201604634.

[12] E. Bindini, M. de los A. Ramirez, X. Rios, U. Cossío, C. Simó, V. Gomez-Vallejo, G. Soler-Illia, J. Llop, S.E. Moya, In Vivo Tracking of the Degradation of Mesoporous Silica through 89Zr Radio-Labeled Core–Shell Nanoparticles, Small. 17 (2021) 2101519. https://doi.org/https://doi.org/10.1002/smll.202101519.

[13] M. de los Á. Ramírez, E. Bindini, P. Moretti, G.J.A.A. Soler Illia, H. Amenitsch, P. Andreozzi, M.G. Ortore, S.E. Moya, Impact of PEGylation on the degradation and pore organization in mesoporous silica nanoparticles: A study of the inner mesoporous structure in physiologically relevant ionic conditions, Colloids Surfaces B Biointerfaces. 219 (2022) 112797. https://doi.org/https://doi.org/10.1016/j.colsurfb.2022.112797.

[14] E. Bindini, Z. Chehadi, M. Faustini, P.-A. Albouy, D. Grosso, A. Cattoni, C. Chanéac, O. Azzaroni, C. Sanchez, C. Boissière, Following in Situ the Degradation of Mesoporous Silica in Biorelevant Conditions: At Last, a Good Comprehension of the Structure Influence, ACS Appl. Mater. Interfaces. 12 (2020) 13598–13612. https://doi.org/10.1021/acsami.9b19956.

[15] S. Goel, F. Chen, S. Luan, H.F. Valdovinos, S. Shi, S.A. Graves, F. Ai, T.E. Barnhart, C.P. Theuer, W. Cai, Engineering Intrinsically Zirconium-89 Radiolabeled Self-Destructing Mesoporous Silica Nanostructures for In Vivo Biodistribution and Tumor Targeting Studies, Adv. Sci. 3 (2016) 1600122. https://doi.org/https://doi.org/10.1002/advs.201600122.

[16] K.S. Finnie, D.J. Waller, F.L. Perret, A.M. Krause-Heuer, H.Q. Lin, J. V Hanna, C.J. Barbé, Biodegradability of sol–gel silica microparticles for drug delivery, J. Sol-Gel Sci. Technol. 49 (2009) 12–18. https://doi.org/10.1007/s10971-008-1847-4.

[17] C.-Y. Lin, C.-M. Yang, M. Lindén, Dissolution and morphology evolution of mesoporous silica nanoparticles under biologically relevant conditions, J. Colloid Interface Sci. 608 (2022) 995–1004. https://doi.org/https://doi.org/10.1016/j.jcis.2021.09.164.

[18] K. Möller, T. Bein, Degradable Drug Carriers: Vanishing Mesoporous Silica Nanoparticles, Chem. Mater. 31 (2019) 4364–4378. https://doi.org/10.1021/acs.chemmater.9b00221.

[19] N. Mendez, A. Liberman, J. Corbeil, C. Barback, R. Viveros, J. Wang, J. Wang-Rodriguez, S.L. Blair, R. Mattrey, D. Vera, W. Trogler, A.C. Kummel, Assessment of in vivo systemic toxicity and biodistribution of iron-doped silica nanoshells, Nanomedicine Nanotechnology, Biol. Med. 13 (2017) 933–942. https://doi.org/https://doi.org/10.1016/j.nano.2016.10.018.

[20] L. Li, F. Tang, H. Liu, T. Liu, N. Hao, D. Chen, X. Teng, J. He, In Vivo Delivery of Silica Nanorattle Encapsulated Docetaxel for Liver Cancer Therapy with Low Toxicity and High Efficacy, ACS Nano. 4 (2010) 6874–6882. https://doi.org/10.1021/nn100918a.

[21] E.M. Björk, P. Mäkie, L. Rogström, A. Atakan, N. Schell, M. Odén, Formation of block-copolymer-templated mesoporous silica, J. Colloid Interface Sci. 521 (2018) 183–189. https://doi.org/https://doi.org/10.1016/j.jcis.2018.03.032.

[22] L. Spitzmüller, F. Nitschke, B. Rudolph, J. Berson, T. Schimmel, T. Kohl, Dissolution control and stability improvement of silica nanoparticles in aqueous media, J. Nanoparticle Res. 25 (2023) 40. https://doi.org/10.1007/s11051-023-05688-4.

[23] H. Yamada, C. Urata, Y. Aoyama, S. Osada, Y. Yamauchi, K. Kuroda, Preparation of Colloidal Mesoporous Silica Nanoparticles with Different Diameters and Their Unique Degradation Behavior in Static Aqueous Systems, Chem. Mater. 24 (2012) 1462–1471. https://doi.org/10.1021/cm3001688.

[24] Q. He, J. Shi, M. Zhu, Y. Chen, F. Chen, The three-stage in vitro degradation behavior of mesoporous silica in simulated body fluid, Microporous Mesoporous Mater. 131 (2010) 314–320. https://doi.org/https://doi.org/10.1016/j.micromeso.2010.01.009.

[25] D. Shen, J. Yang, X. Li, L. Zhou, R. Zhang, W. Li, L. Chen, R. Wang, F. Zhang, D. Zhao, Biphase Stratification Approach to Three-Dimensional Dendritic Biodegradable Mesoporous Silica Nanospheres, Nano Lett. 14 (2014) 923–932. https://doi.org/10.1021/nl404316v.

[26] V. Cauda, A. Schlossbauer, T. Bein, Bio-degradation study of colloidal mesoporous silica nanoparticles: Effect of surface functionalization with organo-silanes and poly(ethylene glycol), Microporous Mesoporous Mater. 132 (2010) 60–71. https://doi.org/https://doi.org/10.1016/j.micromeso.2009.11.015.

[27] B. Gouze, J. Cambedouzou, S. Parrès-Maynadié, D. Rébiscoul, How hexagonal mesoporous silica evolves in water on short and long term: Role of pore size and silica wall porosity, Microporous Mesoporous Mater. 183 (2014) 168–176. https://doi.org/https://doi.org/10.1016/j.micromeso.2013.08.041.

[28] E. Yamamoto, S. Mori, A. Shimojima, H. Wada, K. Kuroda, Fabrication of colloidal crystals composed of pore-expanded mesoporous silica nanoparticles prepared by a controlled growth method, Nanoscale. 9 (2017) 2464–2470. https://doi.org/10.1039/c6nr07416b.

[29] K. Möller, J. Kobler, T. Bein, Colloidal suspensions of nanometer-sized mesoporous silica, Adv. Funct. Mater. 17 (2007) 605–612. https://doi.org/10.1002/adfm.200600578.

[30] A. Barbara, T. Lopez-Rios, S. Dumont, F. Gay, P. Quémerais, Microscope spectrometer for light scattering investigations, Appl. Opt. 49 (2010) 4193–4201. https://doi.org/10.1364/AO.49.004193.

[31] X. Cattoën, A. Noureddine, J. Croissant, N. Moitra, K. Bürglová, J. Hodačová, O. De Los Cobos, M. Lejeune, F. Rossignol, D. Toulemon, S. Bégin-Colin, B.P. Pichon, L. Raehm, J.-O. Durand, M. Wong Chi Man, Click approaches in sol--gel chemistry, J. Sol-Gel Sci. Technol. 70 (2014) 245–253. https://doi.org/10.1007/s10971-013-3155-x.

[32] J. Rouquerol, F. Rouquerol, P. Llewellyn, G. Maurin, K. Sing, Adsorption by powders and

porous solids: principles, methodology and applications, Academic press, 2013.

[33] R. Alvarado Meza, T. Santori, X. Cattoën, A kinetic approach to the mechanism of formation of mesoporous silica nanoparticles, J. Sol-Gel Sci. Technol. (2023). https://doi.org/10.1007/s10971-023-06130-w.

[34] C. Bohren, D. Huffman, Absorption and Scattering of Light by Small Particles, 1998. https://doi.org/https://doi.org/10.1002/9783527618156.

[35] R. Rigler, Ü. Mets, J. Widengren, P. Kask, Fluorescence correlation spectroscopy with high count rate and low background: analysis of translational diffusion, Eur. Biophys. J. 22 (1993) 169–175. https://doi.org/10.1007/BF00185777.

[36] H. Qian, E.L. Elson, On the analysis of high order moments of fluorescence fluctuations, Biophys. J. 57 (1990) 375–380. https://doi.org/10.1016/S0006-3495(90)82539-X.

[37] S.S. Perdoor, F. Dubois, A. Barbara, C. Nguyen, L.M.A. Ali, M. Gary-Bobo, I. Hristovska, K. Combet, O. Pascual, G. Micouin, A. Banyasz, Y. Bretonnière, C. Andraud, A. Ibanez, X. Cattoën, Ultrabright Silica-Coated Organic Nanocrystals for Two-Photon In Vivo Imaging, ACS Appl. Nano Mater. 3 (2020) 11933–11944. https://doi.org/10.1021/acsanm.0c02499.

[38] A.J.F. Siegert, M.I. of T.R. Laboratory, On the Fluctuations in Signals Returned by Many Independently Moving Scatterers, Radiation Laboratory, Massachusetts Institute of Technology, 1943. https://books.google.fr/books?id=5PzqGwAACAAJ.

[39] S. Sjöberg, Silica in aqueous environments, J. Non. Cryst. Solids. 196 (1996) 51–57. https://doi.org/https://doi.org/10.1016/0022-3093(95)00562-5.

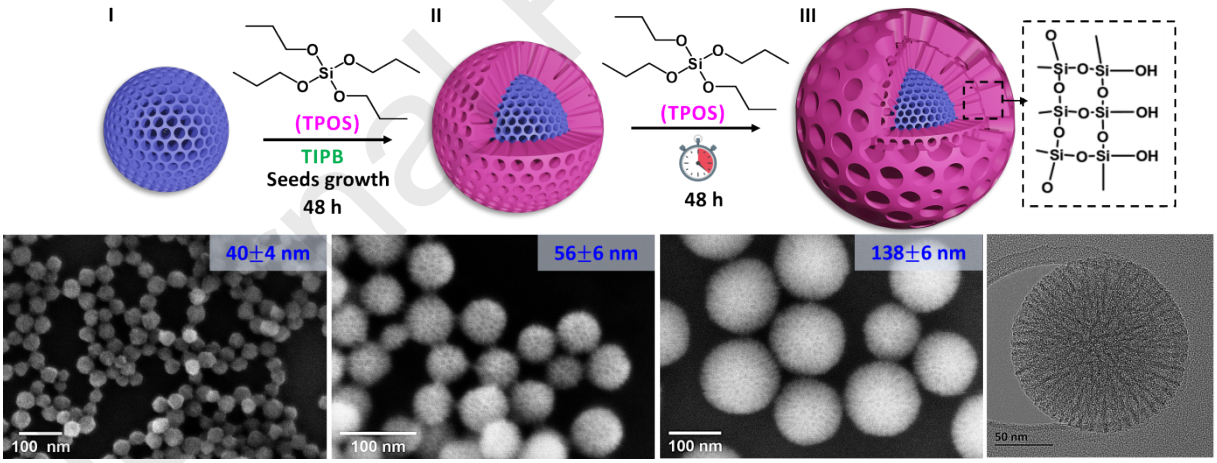

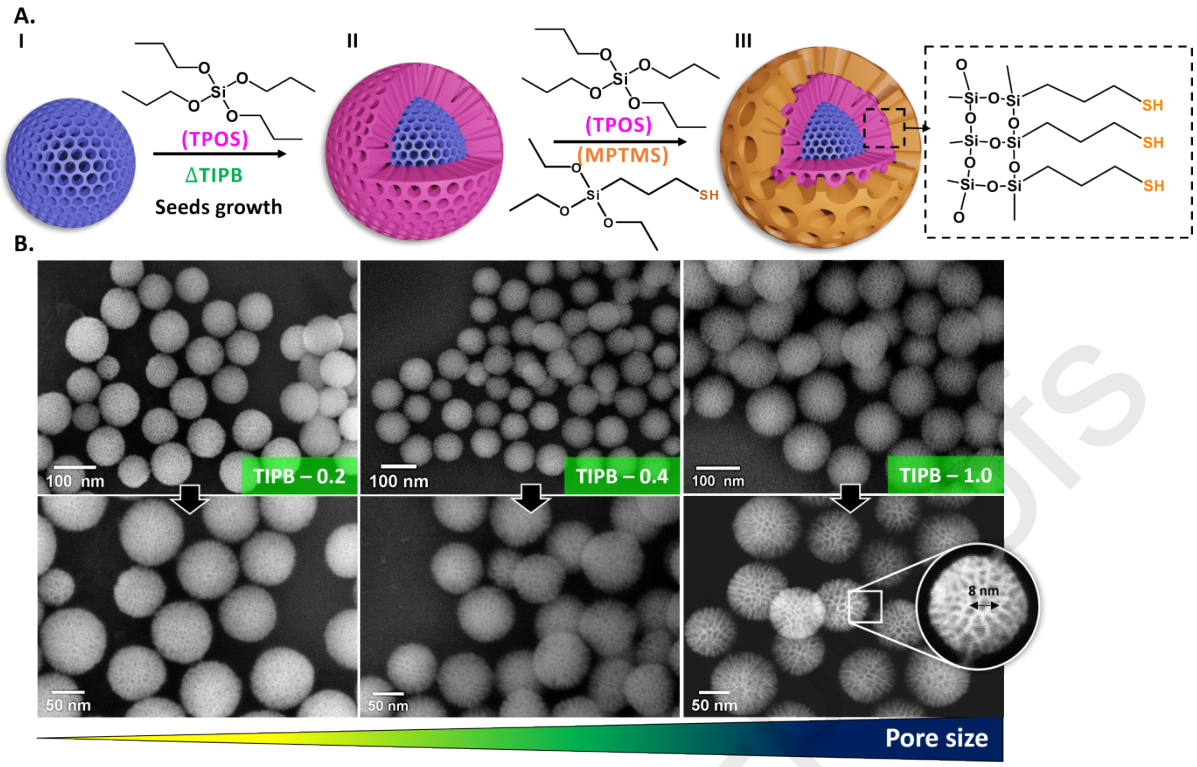

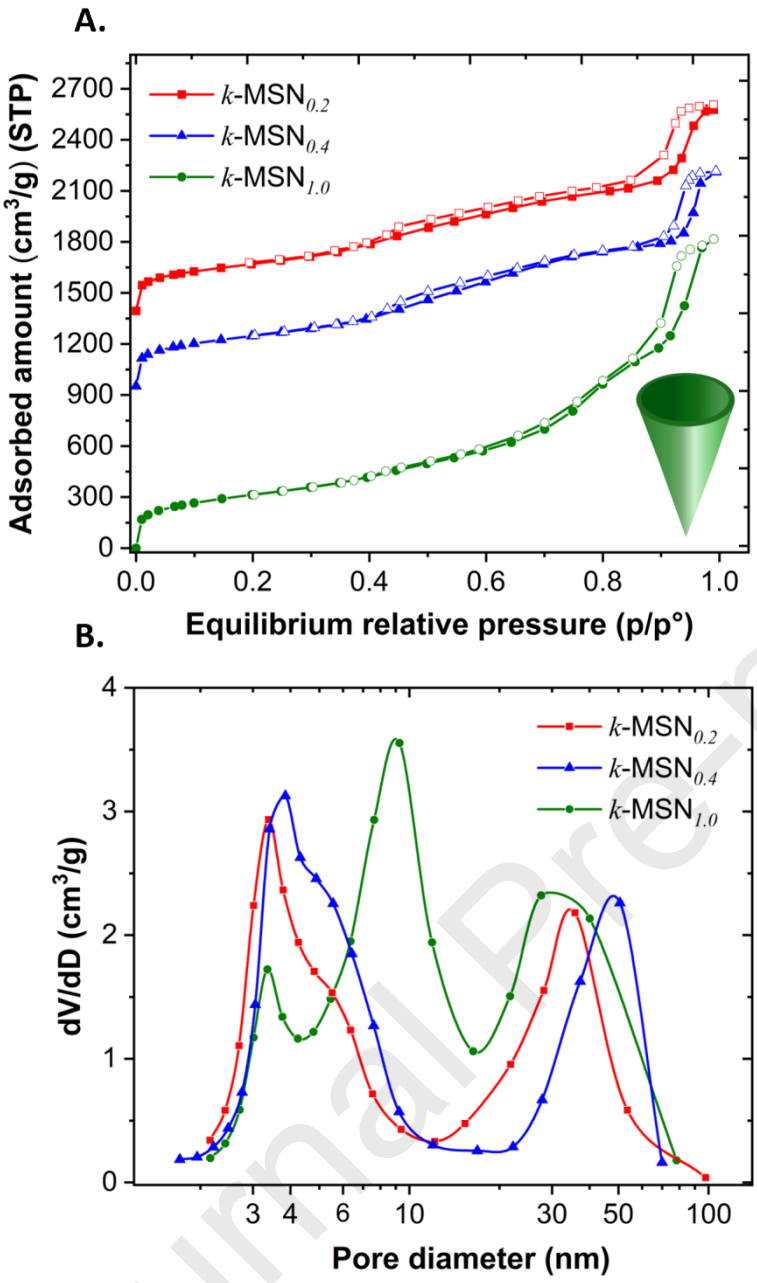

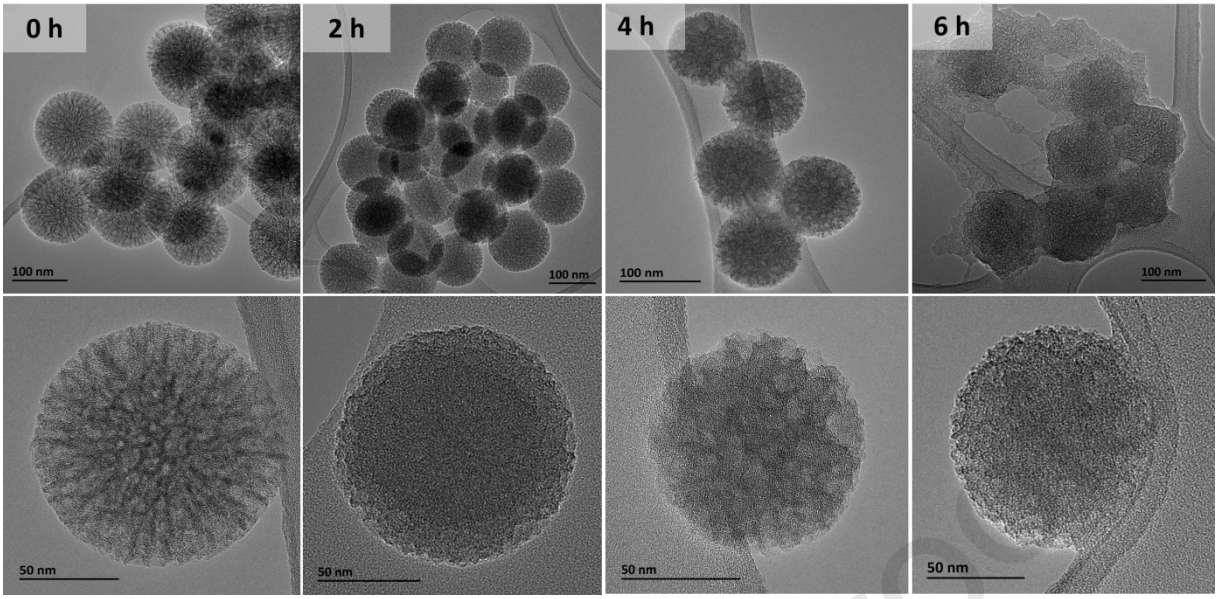

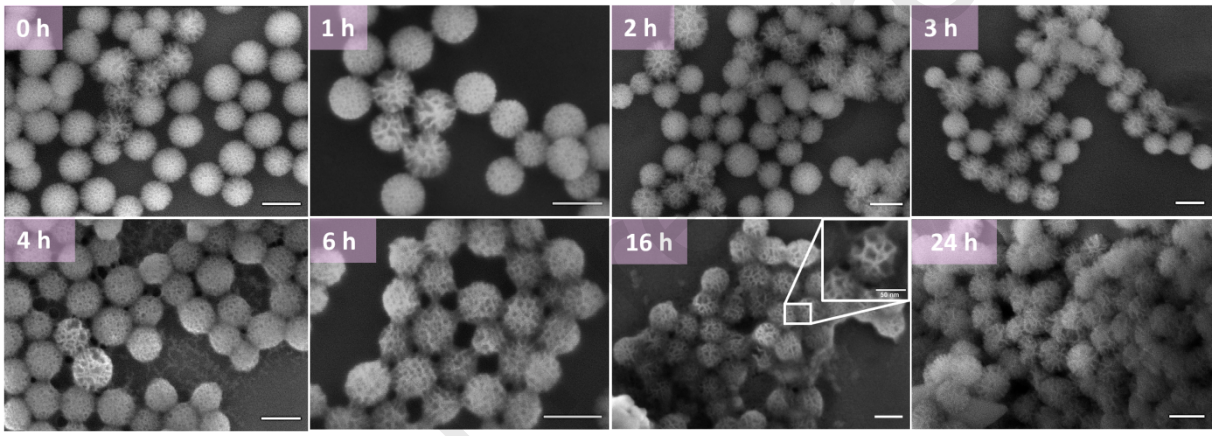

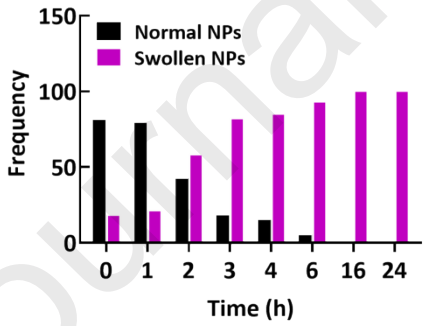

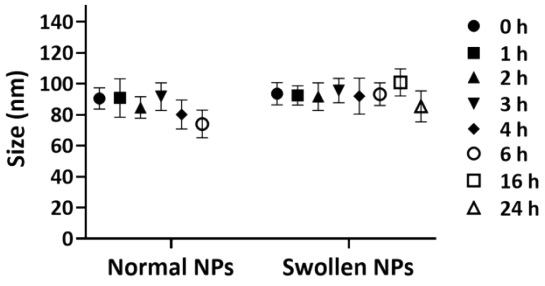

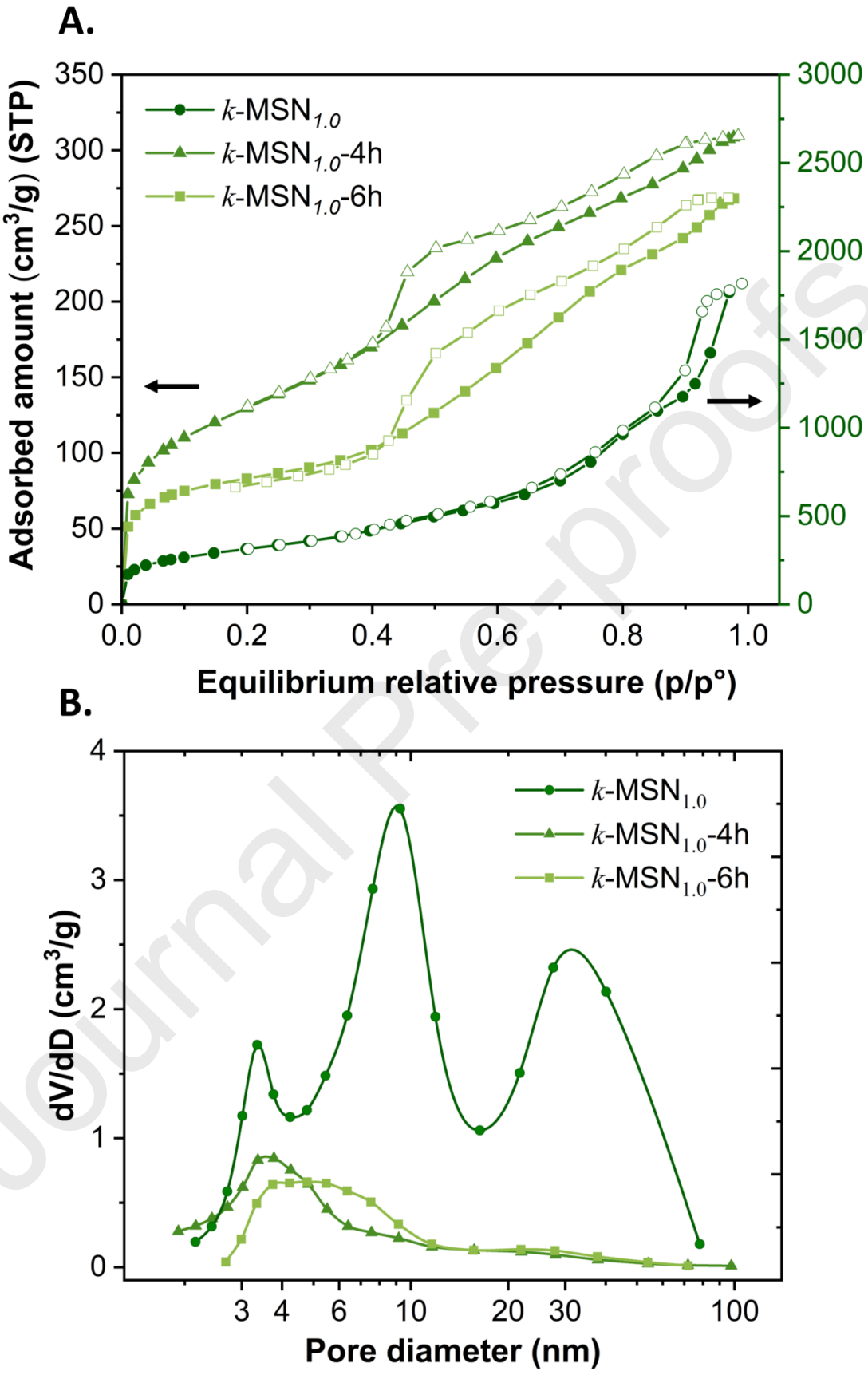

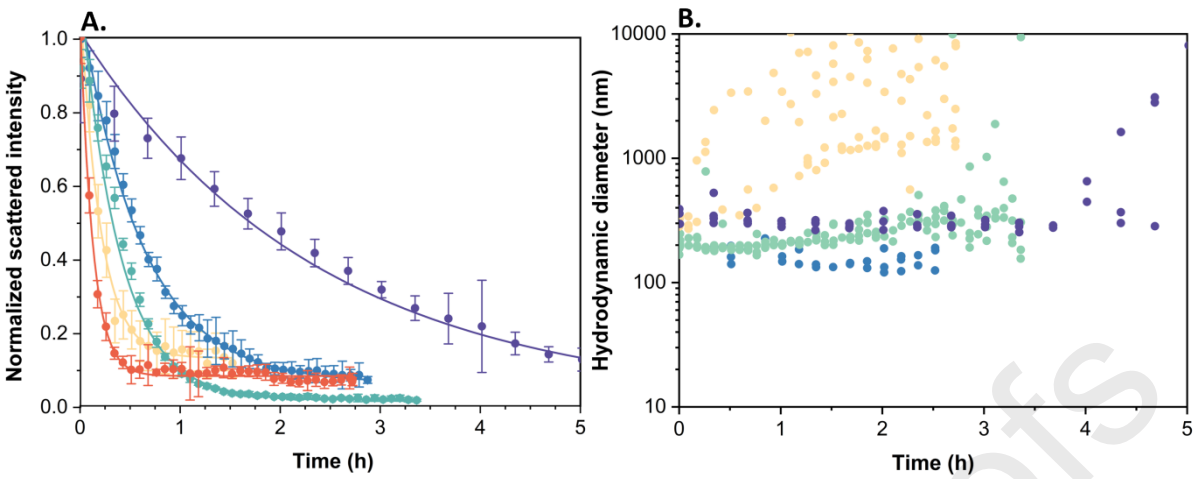

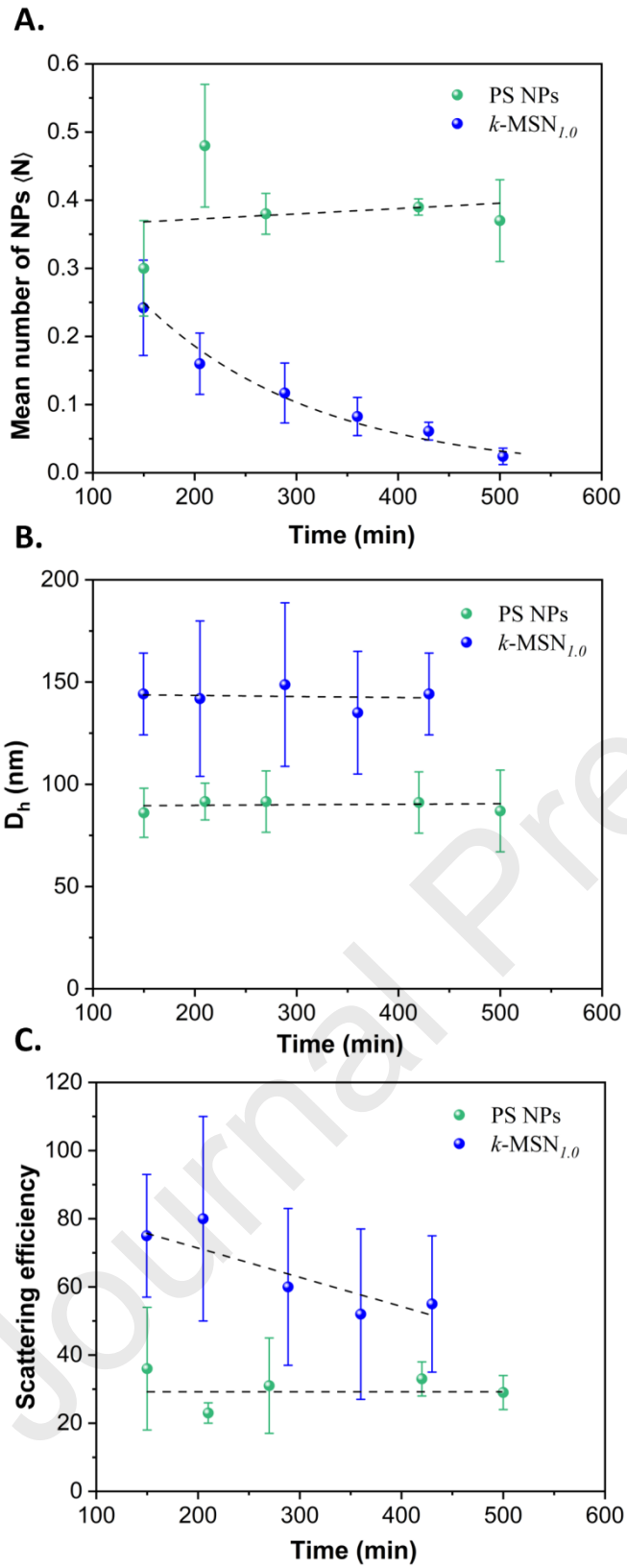

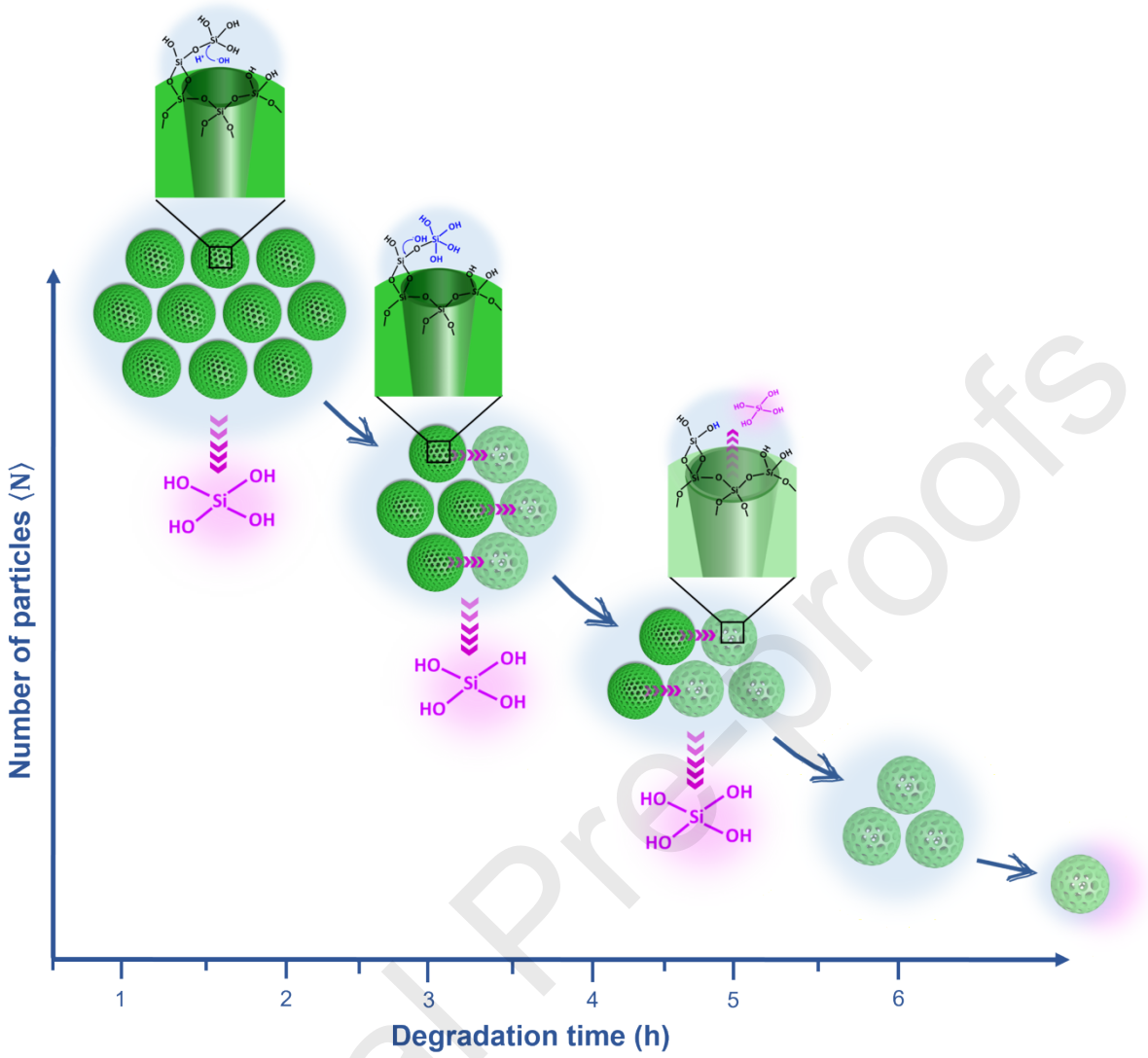

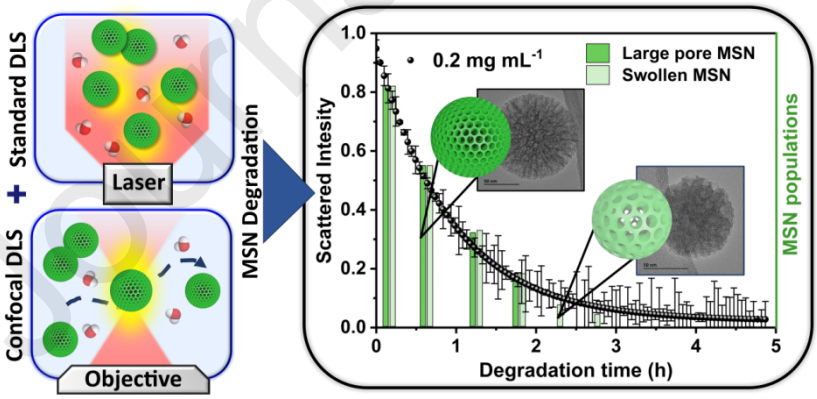

Declaration of interests

☐ The authors declare that they have no known competing financial interests or personal relationships that could have appeared to influence the work reported in this paper.

☒ The authors declare the following financial interests/personal relationships which may be considered as potential competing interests:

Xavier CATTOEN and Farid OUKACINE report financial support was provided by French National Research Agency. If there are other authors, they declare that they have no known competing financial interests or personal relationships that could have appeared to influence the work reported in this paper.